

# Ekman Veering, Internal Waves, and Turbulence Observed under Arctic Sea Ice

SYLVIA T. COLE

*Woods Hole Oceanographic Institution, Woods Hole, Massachusetts*

MARY-LOUISE TIMMERMANS

*Yale University, New Haven, Connecticut*

JOHN M. TOOLE, RICHARD A. KRISHFIELD, AND FREDRIK T. THWAITES

*Woods Hole Oceanographic Institution, Woods Hole, Massachusetts*

(Manuscript received 2 October 2012, in final form 10 December 2013)

## ABSTRACT

The ice–ocean system is investigated on inertial to monthly time scales using winter 2009–10 observations from the first ice-tethered profiler (ITP) equipped with a velocity sensor (ITP-V). Fluctuations in surface winds, ice velocity, and ocean velocity at 7-m depth were correlated. Observed ocean velocity was primarily directed to the right of the ice velocity and spiraled clockwise while decaying with depth through the mixed layer. Inertial and tidal motions of the ice and in the underlying ocean were observed throughout the record. Just below the ice–ocean interface, direct estimates of the turbulent vertical heat, salt, and momentum fluxes and the turbulent dissipation rate were obtained. Periods of elevated internal wave activity were associated with changes to the turbulent heat and salt fluxes as well as stratification primarily within the mixed layer. Turbulent heat and salt fluxes were correlated particularly when the mixed layer was closest to the freezing temperature. Momentum flux is adequately related to velocity shear using a constant ice–ocean drag coefficient, mixing length based on the planetary and geometric scales, or Rossby similarity theory. Ekman viscosity described velocity shear over the mixed layer. The ice–ocean drag coefficient was elevated for certain directions of the ice–ocean shear, implying an ice topography that was characterized by linear ridges. Mixing length was best estimated using the wavenumber of the beginning of the inertial subrange or a variable drag coefficient. Analyses of this and future ITP-V datasets will advance understanding of ice–ocean interactions and their parameterizations in numerical models.

## 1. Introduction

The Arctic Ocean is stratified principally by salinity, with a shallow, nearly vertically uniform mixed layer about 30 m deep in winter bounded below by a strong halocline. The upper Arctic Ocean exchanges heat, salt, and momentum with the overlying sea ice cover. Ice formation releases cold, salty brine to the ocean mixed layer, which in turn can drive vertical convection and cause the mixed layer to deepen. Ice melting releases freshwater to the mixed layer, inducing restratification. Excess heat in the mixed layer, which causes melting,

can result from vertical entrainment of warmer Pacific or Atlantic-origin waters from below the mixed layer or lateral advection of waters warmed by solar radiation absorbed at open leads. Wind forcing creates sea ice motion and so ice–ocean velocity shear, which transfers momentum to the ocean and forces ocean currents and internal waves. The processes of ice formation, ice melt, and ice movement, together with ocean currents and ocean mixing, couple the ice and ocean systems. Changes in sea ice cover are likely to modify vertical turbulent fluxes within the ocean mixed layer and the internal wave field that in turn may have feedbacks on the ice. Thus, we are motivated to improve the understanding of upper-ocean processes and ice–ocean interactions.

Ice–ocean interactions are observed using the first ice-tethered profiler (ITP; [Krishfield et al. 2008a](#); [Toole et al. 2010](#)) to be equipped with a velocity sensor (ITP-V;

---

*Corresponding author address:* Sylvia Cole, Woods Hole Oceanographic Institution, 266 Woods Hole Rd., MS 21, Woods Hole, MA 02543.  
E-mail: [scole@whoi.edu](mailto:scole@whoi.edu)

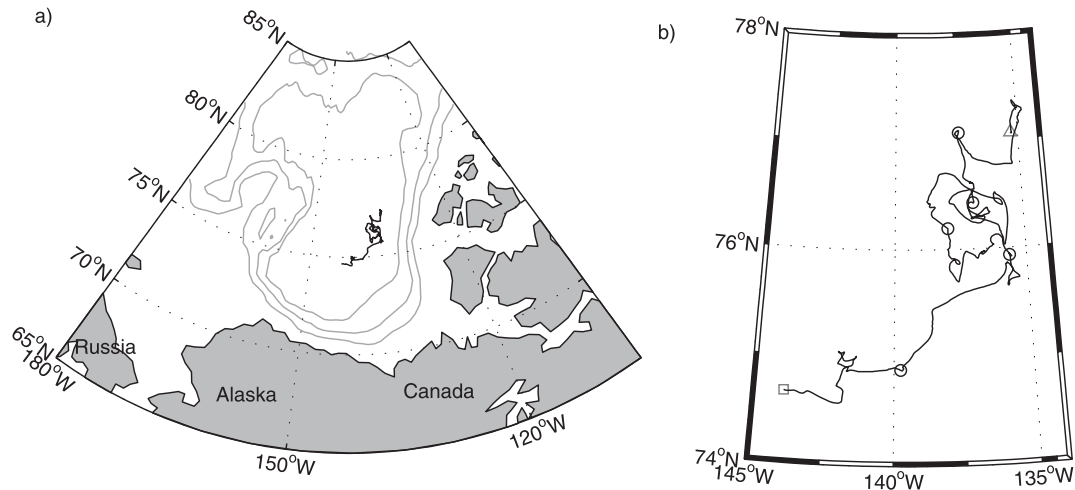


FIG. 1. (a) Map of Canada Basin with the ITP-V drift track in black. Gray contours show 1000-, 2000-, and 3000-m isobaths. (b) Drift track showing location on 9 Oct 2009 (triangle); on 1 Nov, 1 Dec, 1 Jan, 1 Feb, and 1 Mar 2010 (circles); and on 31 Mar 2010 (square).

Williams et al. 2010). The ITP-V instrument provides simultaneous observations of velocity, temperature, and salinity at high vertical and temporal resolution. The first ITP-V returned profiles through the upper ocean as well as measurements of turbulent fluctuations just below the ice–ocean interface. Observations were taken under full ice cover from October 2009 to March 2010 in the Canada Basin. The goal of the present study is to use these data to better understand the ice–ocean system on inertial to seasonal time scales and in doing so demonstrate the utility of the ITP-V.

Inertial motions are common throughout the Arctic and together with tidal motions constitute the majority of the internal wave field (D’Asaro and Morehead 1991; Halle and Pinkel 2003; Pinkel 2005). Ice cover appears to dampen or otherwise impede internal wave activity and vertical mixing as the Arctic internal wave field is observed to be weak compared with ice-free regions (Levine et al. 1985; D’Asaro and Morehead 1991). Internal wave activity can affect water column potential temperature  $\theta$  and salinity  $S$  structure and turbulent fluctuations near the ice–ocean interface. Previous observations where both internal wave velocities and turbulent fluctuations have been observed are primarily from manned drift stations [Surface Heat Budget of the Arctic Ocean (SHEBA), for example; McPhee 2002; Pinkel 2005]; one advantage of the present study is that the internal wave field is analyzed jointly with water column structure and turbulent fluctuations.

Observations of turbulent  $\theta$ ,  $S$ , and velocity fields along with ice velocity allow many commonly used parameterizations to be assessed. Parameters of interest, which have been the focus of many prior studies, include

the turbulent heat flux between the ice and ocean that impacts ice growth and melt (e.g., McPhee 1992), drag between the ice and ocean from which the ocean velocity is derived in numerical models (e.g., McPhee 2002; Shaw et al. 2008), the mixing length or vertical distance over which dominant eddies diffuse momentum (e.g., McPhee 1994), and the turbulent dissipation rate beneath sea ice (e.g., McPhee and Martinson 1994). The ITP-V observations are used to assess these parameterizations, drawing comparisons with and expanding on prior results.

This paper is organized as follows: The ITP-V and its sampling scheme during the first deployment are described in section 2a. Sections 2b and 2c present the calculation of relevant parameters from the observations. An overview of the observations, including a basic description of the Ekman veering, internal wave field, and turbulent fluctuations, is given in section 3a. The impact of internal waves on the water column and turbulent fluxes is presented in section 3b. A joint analysis of heat and salt fluxes is presented in section 3c. Momentum flux parameterizations are presented in section 3d, which includes discussion of the ice–ocean drag coefficient, turbulent dissipation rate, and estimates of mixing length. Conclusions are presented in section 4. The derivation of ocean velocity from the ITP-V platform is detailed in appendix A, and the dominant time and length scales of turbulent fluctuations are detailed in appendix B.

## 2. Observations and methods

### a. ITP-V Sampling scheme

Observations were collected during a 6-month drift of an ITP-V (ITP-35) in the Canada Basin (Fig. 1). The

ITP-V consists of a surface buoy moored in and drifting with the sea ice that supports a weighted wire along which a profiler package crawls (Krishfield et al. 2008a). Deployment was on 9 October 2009 in a floe that was 2.6 m thick, which corresponds to an ice–ocean interface at about 2.3-m depth. In 6 months, the ITP-V drifted anticyclonically within the basin following a circuitous path covering a total distance of 1448 km, with a net displacement of 353 km to the southwest. Sampling ended when the file capacity of the onboard flash drive was reached because real-time data telemetry from this first ITP-V did not occur (the system was recovered to offload the archived data).

Ice velocity, ocean velocity, temperature, and salinity are derived from ITP-V sensor data; wind velocity is derived from a reanalysis wind product. The ITP-V profiler package contained a CTD measuring at 1 Hz, a single-point three-axis current meter measuring at 2 Hz, and attitude/motion sensors measuring at 2 Hz (three-axis angle rate gyro, three-axis accelerometer, and three-axis fluxgate compass). The CTD data were processed according to Krishfield et al. (2008b). The current meter measures velocity relative to the profiler package as it drifts with the ice and crawls along the wire. Absolute ocean velocity,  $u$ ,  $v$ , and  $w$ , is obtained by accounting for 1) the pitch, roll, and heading of the profiler, which are determined from the attitude/motion sensors (Williams et al. 2010); 2) the vertical and horizontal motion of the profiler as it moved along the (possibly inclined) wire, which is estimated using wire angle derived from the attitude sensors and the time rate of change of pressure  $\partial P/\partial t$  as measured by the CTD; and 3) the motion of the entire ITP-V system due to the ice velocity. Further details, including aligning the CTD and velocity records in time as well as calibrations and a discussion of errors, are given in appendix A. Ice velocity,  $u_{\text{ice}}$  and  $v_{\text{ice}}$ , is derived from hourly GPS fixes and linearly interpolated in time to align with the time of the ITP-V observations. Atmospheric winds are derived from the 6-h National Centers for Environmental Prediction (NCEP) reanalysis wind product (Kalnay et al. 1996). Surface wind velocity is interpolated in space and time to align with the ITP-V observations.

Sampling consisted of vertical profiles interspersed by periods of parked measurements near the ice–ocean interface. Profiles were obtained every 4 h to 150-m depth, with two of those profiles per day extending to 750-m depth. The 2-Hz velocity observations and 1-Hz CTD observations with 12.5- and 25-cm vertical resolution, respectively (the nominal profiler speed along the wire was  $0.25 \text{ m s}^{-1}$ ), are averaged into 1-m depth bins. The shallowest depth bin consistently observed while profiling was 7 m. Twice daily between profiling

operations, the ITP-V was programmed to park at a fixed position along the wire near 6-m depth and sample for approximately 40 min to observe turbulent fluctuations. Parked measurements were at a mean depth plus or minus one standard deviation of  $5.7 \pm 0.4 \text{ m}$ , about 3.0–3.8 m below the initial ice–ocean interface. Each approximately 40-min record was sufficiently long to capture the dominant time scales (100–200 s) and horizontal length scales (5–50 m) of the eddies responsible for vertical fluxes of heat, salt, and momentum (appendix B). Noise was evident at periods less than 10 s (appendix B); fluctuations at periods less than 10 s are excluded from analysis. The final data product for the fixed-depth observations is at the 1-Hz rate of the CTD observations. This study primarily focuses on the more frequently sampled upper 150 m of the water column and the turbulent fluctuations below the ice–ocean interface.

### b. Parameters from profile data

Mixed layer and mixing layer depths are defined using critical density differences from the shallowest depth bin. The mixed layer base is defined using a critical density difference of  $0.25 \text{ kg m}^{-3}$ ; thresholds ranging from 0.1 to  $0.5 \text{ kg m}^{-3}$  produced essentially the same mixed layer base. The mixing layer base is defined using a critical density difference of  $0.01 \text{ kg m}^{-3}$  to delineate that portion of the mixed layer that had been recently homogenized in the vertical.

An Ekman depth was determined for each velocity profile. Under steady-state conditions, constant viscosity, and neutral buoyancy, the Ekman spiral with a northward surface stress is described by

$$u_{\text{Ekman}} = V_0 e^{-z/D_E} \cos(45^\circ - z/D_E) \quad \text{and} \quad (1a)$$

$$v_{\text{Ekman}} = V_0 e^{-z/D_E} \sin(45^\circ - z/D_E), \quad (1b)$$

where  $V_0$  is the ocean surface velocity,  $D_E$  is the Ekman depth, and  $z$  is depth positive downward (Ekman 1905). The velocity magnitude was fit to an exponential decay:

$$\{[u(z) - u_{\text{ref}}]^2 + [v(z) - v_{\text{ref}}]^2\}^{1/2} = V_0 e^{-z/D_E}, \quad (2)$$

where  $V_0$  and  $D_E$  are the fitted parameters, and  $u_{\text{ref}}$  and  $v_{\text{ref}}$  constitute a reference velocity. The reference velocity is taken to be the velocity 2 m above the base of the mixing layer to consider only profile segments with negligible stratification. The fit is from the shallowest depth bin to 3 m above the base of the mixing layer. The effective Ekman viscosity  $\kappa_E$  is calculated from the relation  $D_E = \sqrt{2\kappa_E/f}$ , where  $f$  is the Coriolis parameter.

Rotary spectra of velocity are considered as a function of frequency and of vertical wavenumber. Frequency

spectra are calculated for the ice velocity and ocean velocity at each depth bin. Ice velocity is first linearly interpolated to a uniform 1-h grid, and ocean velocity at each depth bin to a uniform 4-h grid. Vertical wavenumber spectra are calculated for each profile using velocity between 40- and 150-m depth. Rotary spectra are calculated by removing a mean and trend from each record (velocity as a function of time or depth), taking the Fourier transform, and averaging the resulting Fourier coefficients in frequency or vertical wavenumber space.

### c. Parameters from parked measurements

Heat, salt, and momentum fluxes are estimated for each approximately 40-min fixed-depth record. Heat and salt fluxes are calculated as  $\rho C_p \langle \theta' w' \rangle$  and  $(\rho/1000) \langle S' w' \rangle$ , respectively, where  $\rho$  is density, and  $C_p$  is specific heat capacity. Momentum flux magnitude is presented in terms of the friction velocity:

$$u_* = (\langle u' w' \rangle^2 + \langle v' w' \rangle^2)^{1/4}. \quad (3)$$

Primed quantities indicate the removal of a mean and trend from each approximately 40-min record after a 10-s low-pass filter is applied (e.g., Fig. B1, described in greater detail below), and angle brackets indicate an average over each approximately 40-min record. Positive fluxes correspond to warm/salty water traveling upward or cold/freshwater traveling downward.

The production of turbulent kinetic energy (TKE),  $-\langle u' w' \rangle \partial \langle u \rangle / \partial z - \langle v' w' \rangle \partial \langle v \rangle / \partial z$ , was estimated using  $\partial \langle u \rangle / \partial z = (u_{\text{ice}} - \langle u_6 \rangle) / \langle z_m \rangle$ , where  $u_6$  indicates the velocity from parked measurements at 6-m depth, and  $z_m$  is the distance from the ice–ocean interface to the measurement depth. The ice–ocean interface is taken to be at 2.3-m depth. Using the ice–ocean velocity difference and not the local ocean velocity shear may overestimate TKE production.

Horizontal wavenumber  $k$  is derived assuming a frozen field hypothesis as frequency divided by the magnitude of the mean relative velocity past the sensor over each 40-min sampling period. Mean relative velocity past the sensor is equivalent to the ice–ocean velocity difference  $[(u_6 - u_{\text{ice}})^2 + (v_6 - v_{\text{ice}})^2]^{1/2}$  as the sensor is advected with the ice velocity and represents the speed at which turbulent eddies are advected past the velocity sensor. Under a frozen field hypothesis, larger relative velocities translate to a larger horizontal distance observed by the ITP-V during a 40-min sampling period.

Horizontal wavenumber spectra  $E(k)$  are used to derive two estimates of the turbulent dissipation rate and the wavenumber that indicates the beginning of the inertial subrange. Horizontal wavenumber spectra were

calculated after the relative velocity for each 40-min sampling interval ( $u_6 - u_{\text{ice}}$ ,  $v_6 - v_{\text{ice}}$ , and  $w_6$ ) was rotated into an along-stream, across-stream, and nearly vertical coordinate system such that each 40-min-mean relative across-stream and vertical velocity was zero.

The beginning of the inertial subrange is identified from the spectra of vertical velocity. Similar to previous studies (McPhee and Martinson 1994; MCPhee 1994, 2002, 2004), a seventh-order polynomial was fit to  $kE(k)$  calculated from vertical velocity fluctuations for wavenumbers corresponding to frequencies less than 0.4 cycles per second (cps), and the beginning of the inertial subrange  $k_{\text{max}}$  was identified as the maximum of this polynomial fit.

The turbulent dissipation rate is estimated using two methods. The inertial dissipation method assumes a balance between TKE production and dissipation (Tennekes and Lumley 1972; Gross and Norwell 1985):

$$E(k) = \alpha \varepsilon_1^{2/3} k^{-5/3} + n, \quad (4a)$$

where  $\varepsilon_1$  is the turbulent dissipation rate estimate,  $n$  is white noise, and  $\alpha$  is the Kolmogorov constant taken to be 0.5 in the along-stream direction (Huntley 1988) and  $(4/3) \times 0.5$  in the across-stream and vertical directions consistent with isotropic turbulence (Tennekes and Lumley 1972). Wavenumber spectra for each 40-min record were fit to (4a) for wavenumbers corresponding to frequencies of 0.02–0.2 cps. These frequencies were chosen to be above the noise floor of the observations. A second method makes no assumptions about the TKE equation (McPhee and Martinson 1994; MCPhee 2004):

$$k_i E(k_i) = \alpha \varepsilon_2^{2/3} k_i^{-2/3}, \quad (4b)$$

where  $\varepsilon_2$  is the turbulent dissipation rate estimate, and  $k_i$  is any specific horizontal wavenumber in the inertial subrange. Using the seventh-order polynomial fit of  $kE(k)$ , a wavenumber corresponding to 75% of  $k_{\text{max}} E(k_{\text{max}})$  was used in (4b), provided it was larger than  $k_{\text{max}}$  and smaller than a wavenumber corresponding to a frequency of 0.4 cps (87% of spectra fulfilled this criteria).

## 3. Results and discussion

### a. Overview

This subsection presents an overview of the observations using an approach from top to bottom and from large to small scale. The winds, ice velocity, and upper-ocean velocity are introduced, followed by the temperature, salinity, and velocity profiles, and Ekman currents, internal waves, and turbulent fluctuations.

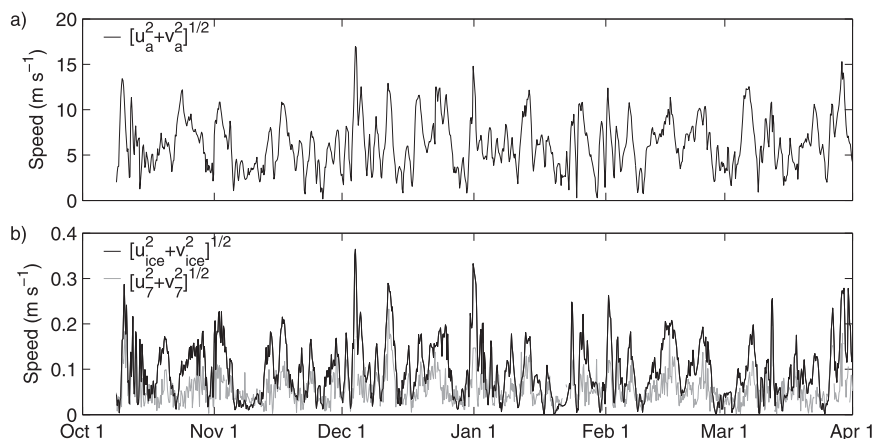


FIG. 2. (a) Wind speed and (b) ice speed (black) and 7-m ocean speed (gray). Wind speed is interpolated in space and time from 6-h NCEP reanalysis surface winds to the 4-h ocean velocity record. Ice speed is calculated from the 1-h record of GPS position and then interpolated in time to match the 4-h ocean velocity record.

Surface winds ( $u_a$ ,  $v_a$ ), ice velocity ( $u_{ice}$ ,  $v_{ice}$ ), and ocean velocity at 7-m depth ( $u_7$ ,  $v_7$ ) are first considered in terms of their speed (Fig. 2). Ice and ocean speeds exhibited greater energy on smaller temporal scales, such as those of tidal and inertial motions, than did wind speed as these higher-frequency motions were heavily smoothed in the NCEP wind product. Over the 6 months of observations, speeds had a median plus or minus one standard deviation of  $5.9 \pm 2.8 \text{ m s}^{-1}$  for the surface wind,  $0.09 \pm 0.06 \text{ m s}^{-1}$  for the ice, and  $0.05 \pm 0.03 \text{ m s}^{-1}$  for the ocean at 7-m depth. The wind and ice speeds have a best-fit relationship of  $u_{ice} = 0.019u_a$ , close to the free-drift ratio of 0.02 and the ratio observed during SHEBA, but different from the winter ratio observed during the Arctic Ice Dynamics Joint Experiment (AIDJEX) that was less than 0.01 (McPhee 2002). The speed regression between the ice and ocean at 7-m depth is  $u_7 = 0.43u_{ice}$ . There was good correlation over the entire 6-month record between wind speed, ice speed, and ocean speed, consistent with winds that forced ice motion, which in turn forced ocean mixed layer currents.

The acquired temperature and salinity profiles showed conditions typical of the Canada Basin in winter (Figs. 3a,b). Stratification was almost entirely determined by salinity, with a strong halocline at the base of the surface mixed layer and relatively weak vertical gradients below 300-m depth. Mixed layer depth varied from 15 to 40 m, with the shallowest depths observed in October. Within the mixed layer, the water column was only occasionally truly well mixed; imbedded shallower mixing layers were frequently observed (Fig. 3b; see also Timmermans et al. 2012). The layer of relatively warm water near 50-m depth is Pacific Summer Water and is isolated from the mixed layer by the strong stratification at the mixed

layer base. A few profiles, particularly in November, show a near-surface temperature maximum (Maykut and McPhee 1995; Jackson et al. 2010) immediately below the mixed layer base at around 30-m depth. The Atlantic water temperature maximum is evident below 250-m depth.

Profiles of absolute ocean velocity (Figs. 3c,d) reveal Ekman-like shear in the mixed layer, inertial and tidal currents throughout the water column, and weak geostrophic velocities. Ocean velocity was typically less than  $0.1 \text{ m s}^{-1}$  in magnitude and rarely in the same direction for more than a day or so. The largest ocean currents of about  $0.4 \text{ m s}^{-1}$  were associated with an anticyclonic eddy observed in March whose baroclinic structure brought warmer water closer to the mixed layer base. Other anticyclonic eddies in this depth range were also observed, but for shorter periods of time, and were associated with spreading isopycnals and colder temperatures (e.g., temperature and velocity on 29 November). With the exception of such eddies, ocean current speeds were largest near the surface but smaller in magnitude than ice floe speeds. The largest velocity shears were between the ice and uppermost ocean velocity observation and about the mixed layer base.

Ekman spiraling is investigated with ITP-V profile data by rotating wind and ocean velocity into a coordinate system aligned with the direction of the ice velocity at the time of each profile. Ekman spiraling was apparent in individual profiles; for most profiles, ice velocity was directed  $0^\circ$ – $90^\circ$  to the right of the winds, and ocean velocity at 7-m depth was directed  $0^\circ$ – $90^\circ$  to the right of ice velocity (Figs. 4a,b). The smallest wind or ocean velocities, those less than 3 or  $0.05 \text{ m s}^{-1}$ , respectively, were least likely to have consistent angular offsets

between the wind and ice velocities or between the ice and ocean velocities. The median angle between the surface winds and ice velocity was  $28^\circ$  for wind speeds in excess of  $3 \text{ m s}^{-1}$ , and that between the ice velocity and ocean velocity at 7-m depth was  $35^\circ$  for ocean speeds in excess of  $0.05 \text{ m s}^{-1}$ . The wind and ocean velocities were measured at different relative depths within their respective Ekman layers and so are expected to have different median rotation angles. A mean profile is constructed by averaging all profiles with 7-m ocean speeds in excess of  $0.05 \text{ m s}^{-1}$  (Fig. 4c). The mean profile shows ice velocity directed to the right of the wind vector, ocean currents directed to the right of the ice velocity, and ocean currents that rotate to the right and decay with depth in the mixed layer. This is in good agreement with the classic Ekman spiral and previous observations (Hunkins 1966; Shaw et al. 2008). Deviations from a classic Ekman spiral appear around 15–20-m depth, coincident with the shallowest mixing layer bases, suggesting that stratification influences these currents. Average Ekman currents were the same magnitude as instantaneous mixed layer currents, suggesting Ekman veering was a dominant process within the mixing layer (and presumably mixed layer).

Ekman depth was calculated using (2) for 90% of the profiles in which velocity magnitude decayed with depth (e.g., Fig. 5a). A well-defined Ekman layer did not always occur when ocean speeds were small (e.g., Fig. 4b) or when the ice speed and mixed layer velocity were rapidly changing in time. The median estimated Ekman depth was 11 m, with a distribution skewed toward smaller values such that 50% of Ekman depths were between 6 and 17 m (Fig. 5b), smaller than most mixing layer depths. These values are similar to those found previously under sea ice (Hunkins 1966; McPhee 1987; McPhee and Martinson 1994; McPhee 2008a).

Near-inertial and tidal motions were notable throughout the observation period in both ice and ocean velocity. Rotary spectra of ice velocity and ocean velocity at all depths had a peak near the semidiurnal period in the clockwise component only (Fig. 6a). The peak encompasses the 12.0- and 12.42-h period semidiurnal tidal motions as well as near-inertial motions: the inertial period at the measurement latitudes of  $74.6^\circ$ – $77.4^\circ\text{N}$  ranges between 12.30 and 12.45 h. No attempt is made here to distinguish tidal from near-inertial motions. We note that ocean velocity spectra flatten at frequencies higher than about 1 cycle per day (cpd) (most evident in the counterclockwise component) because the ITP was programmed to profile at the 4-h period, resulting in a few kilometers separation between profiles. Higher-frequency motions including internal waves and low-frequency spatial variations are aliased and Doppler

smearred into frequencies higher than 1 cpd [an underwater glider has similar temporal resolution and aliasing effects (Rudnick and Cole 2011)]. Ice velocity is unaffected, which in part occurs because of its higher 1-h temporal resolution and in part suggests that high-frequency internal waves do not significantly affect ice motion. Rotary spectra of the vertical shear of horizontal velocity below the mixed layer also show a peak near the semidiurnal period in the clockwise component only, indicative of near-inertial and tidal internal waves (Fig. 6c).

Upward and downward energy propagation by the internal wave field can be distinguished using rotary spectra in vertical wavenumber space. Averaged over all profiles, clockwise-with-depth velocity and shear variances were slightly elevated over counterclockwise velocity and shear variances for wavelengths greater than about 10 m (Figs. 6b,d). The elevated clockwise variance indicates a slight dominance of downward internal wave propagation, consistent with local generation of internal waves near the surface. Similar in shape to previous Arctic observations (D'Asaro and Morehead 1991; Merrifield and Pinkel 1996; Pinkel 2005), and different from the classic Garrett–Munk description (Cairns and Williams 1976; Gregg and Kunze 1991), the deployment-mean ITP-V shear spectrum exhibits a peak at 10–50-m vertical wavelength; note also the noise at wavelengths less than about 8 m.

Turbulent fluctuations were observed at 6-m depth near the top of the Ekman layer. Early in the deployment, this measurement depth was 3.4 m below the ice–ocean interface; ice growth during winter brought the ice–ocean interface closer [typical winter ice growth is around 70 cm (Perovich and Richter-Menge 2009)]. A boundary layer is assumed with velocity that varies logarithmically to match the ice velocity to the ocean velocity at the top of the Ekman layer. The base of the log layer can be estimated as  $0.05D_E$  (Shaw et al. 2008). For Ekman depths of 5–40 m, which includes most of the observed Ekman depths (Fig. 5b), the vertical extent of the log layer would be about 0.25–2.0 m. Because our observations were about 3 m below the ice–ocean interface, the observed turbulent fluctuations were primarily within the Ekman layer and deeper than any log layer.

The estimated vertical turbulent heat, salt, and momentum fluxes at 6-m depth had a range of values during winter (Fig. 7). The time-mean plus or minus one standard deviation of the friction velocity, heat flux, and salt flux was  $0.007 \pm 0.005 \text{ m s}^{-1}$ ,  $1.0 \pm 2.9 \text{ W m}^{-2}$ , and  $-0.2 \times 10^{-6} \pm 3.9 \times 10^{-6} \text{ kg m}^{-2} \text{ s}^{-1}$ , respectively. Positive and negative salt flux events were about equally likely, while positive heat flux events were larger in

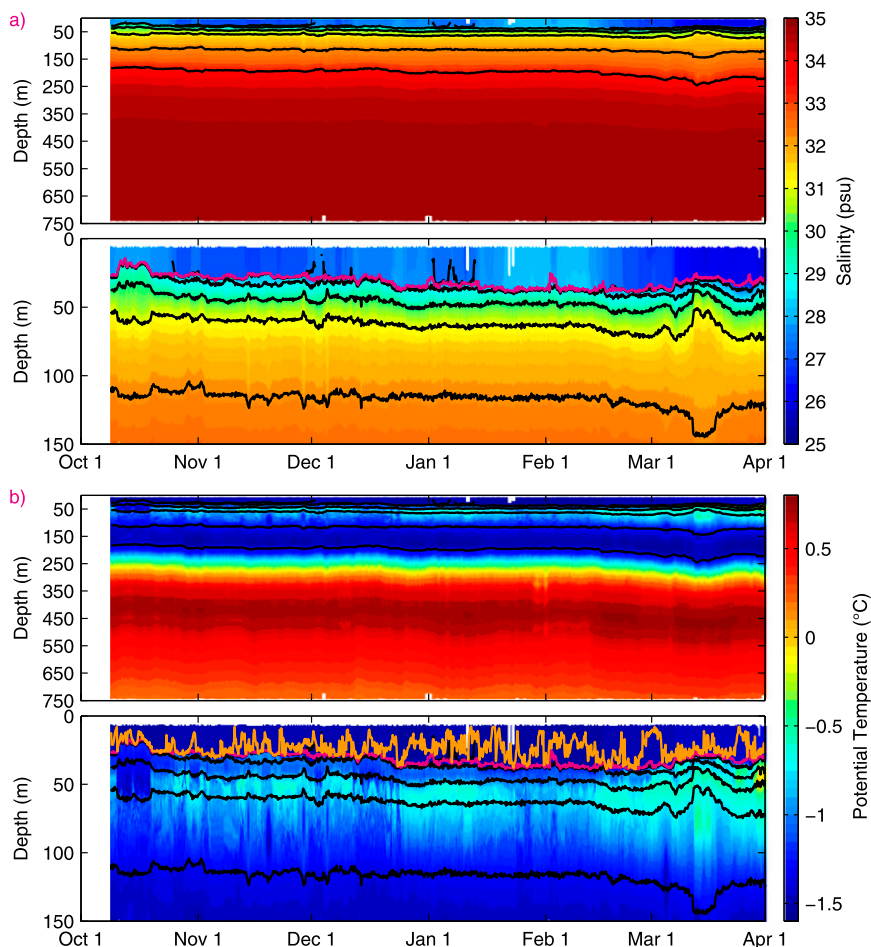


FIG. 3. Depth–time sections of (a) salinity, (b) potential temperature, (c) absolute eastward velocity, and (d) absolute northward velocity. The upper 750 m with 2 profiles per day as well as the upper 150 m with 6 profiles per day are shown. In (c) and (d), ice velocity is shown in a band between  $-3$ - and  $3$ -m depth, and absolute ocean velocity is shown at the observed depths below. Isopycnal depths (black) are spaced apart by  $1.0 \text{ kg m}^{-3}$  ( $22.0$ – $27.0 \text{ kg m}^{-3}$ ). The mixed layer base (magenta) and mixing layer base [orange in (b)] are calculated using thresholds of  $0.25$  and  $0.01 \text{ kg m}^{-3}$  from the shallowest observation, respectively.

magnitude and more frequent than negative heat flux events. Overall, heat and salt fluxes were both dominated by a few large events (see also McPhee 1992).

### b. Impact of internal waves

A segment of the velocity shear record from the end of December captured internal waves that had dominant upward phase propagation with time, consistent with downward energy flux (Fig. 8d). Upward phase propagation was most evident after 23 December and in the upper 80 m. A shift in wind direction (Fig. 8a) and a corresponding shift in the direction of ice–ocean shear (Fig. 8b) occurred on 23–24 December, suggesting that these internal waves were locally generated due to changes in wind forcing and ice–ocean shear. The shift in

winds and ice–ocean shear (and internal waves generated just after 23 December) also corresponded to elevated momentum flux (Fig. 8c) and an erosion of stratification within the mixed layer due to a mixing event that reached to the mixed layer base (Fig. 8e). It is not clear in what order the wind shift, increased turbulence, erosion of mixed layer stratification, and internal wave generation occurred; all events appear to have taken place simultaneously over a 1–2-day period.

Over the entire 6 months of observations, internal wave activity and associated velocity shear were not constant. To examine the near-inertial/tidal frequency motions as a function of depth and time, wavelet coefficients (a Morlet wavelet with  $n = 1$ ) are averaged over 7 days in time and 5 m in depth for frequencies between

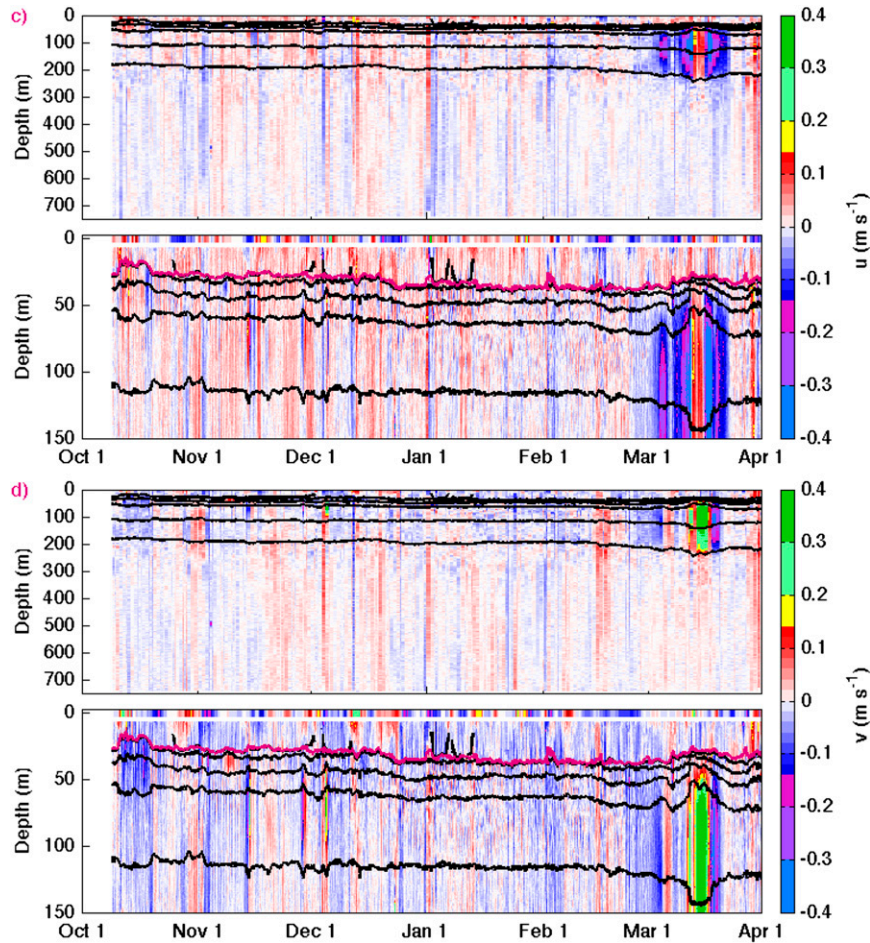


FIG. 3. (Continued)

1/12.0 and 1/12.8 cycles per hour (cph) (Figs. 9b,d). Ice–ocean shear at these frequencies (Fig. 9b) as well as wind speed and friction velocity (Figs. 9a,c) were slightly elevated in December. At all depths below the mixed layer, near-inertial/tidal velocity shear was elevated from 1 December through mid-February, with the region of highest shear about the mixed layer base expanding downward until 1 February (Fig. 9d).

Vertical mixing due to internal waves altered stratification. The December–January period of increased internal wave shear was associated with a somewhat deeper mixed layer and increased stratification within the mixed layer. Increased stratification manifested as more frequent occurrences of shallow mixing layers (Fig. 3b) so that the average mixing layer depth was shallower than the average mixed layer depth (Fig. 9e). More frequent shallow mixing layers suggest that submesoscale restratification (and its relationship with vertical mixing) has a complex behavior under ice cover. Internal wave mixing likely eroded the shallow mixing

layers and not the strong stratification at the mixed layer base.

Internal wave activity was also associated with changes to turbulent fluctuations just below the ice–ocean interface. The December–January period of increased internal wave activity corresponded to predominantly positive salt fluxes, and very little change in cumulative heat flux (Figs. 7b,c). Positive salt fluxes are consistent with turbulent entrainment of saltier waters from below the mixed layer. However, positive heat fluxes did not dominate, consistent with entrainment at the base of the shallower mixing layer where the vertical temperature gradient was weak. In contrast to the December–January period, February and March corresponded to predominantly positive heat fluxes and predominantly negative salt fluxes, consistent with convection from brine rejection during ice formation (cold and salty water sinking). The October–November period of positive heat fluxes and moderate but alternating salt fluxes may reflect the combined action of brine rejection and vertical entrainment.

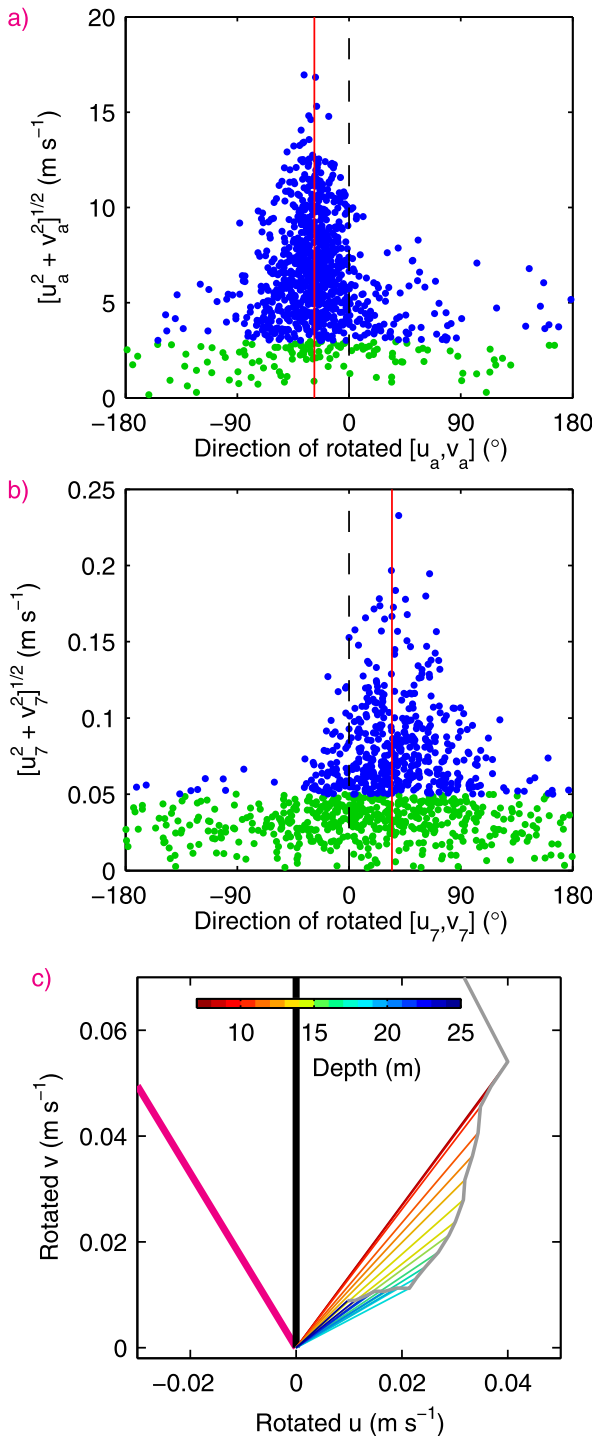


FIG. 4. Velocity statistics in local ice coordinates. Each wind, ice, and ocean velocity observation was rotated into a coordinate system with ice velocity oriented northward (0°). The direction of (a) the rotated surface wind vs wind speed and (b) the rotated 7-m ocean velocity vs 7-m ocean speed. Red lines show the median directions of  $-28^\circ$  for wind speeds greater than  $3 \text{ m s}^{-1}$  in (a) and  $35^\circ$  for ocean speeds greater than  $0.05 \text{ m s}^{-1}$  in (b). Positive angles are to the right of the ice direction. (c) The mean profile for ocean speeds greater than  $0.05 \text{ m s}^{-1}$  with mean wind velocity ( $6.8 \text{ m s}^{-1}$ ) in magenta, mean ice velocity ( $0.13 \text{ m s}^{-1}$ ) directed northward in black, and mean ocean velocity estimates at 1-m depth intervals in color, starting at 7-m depth.

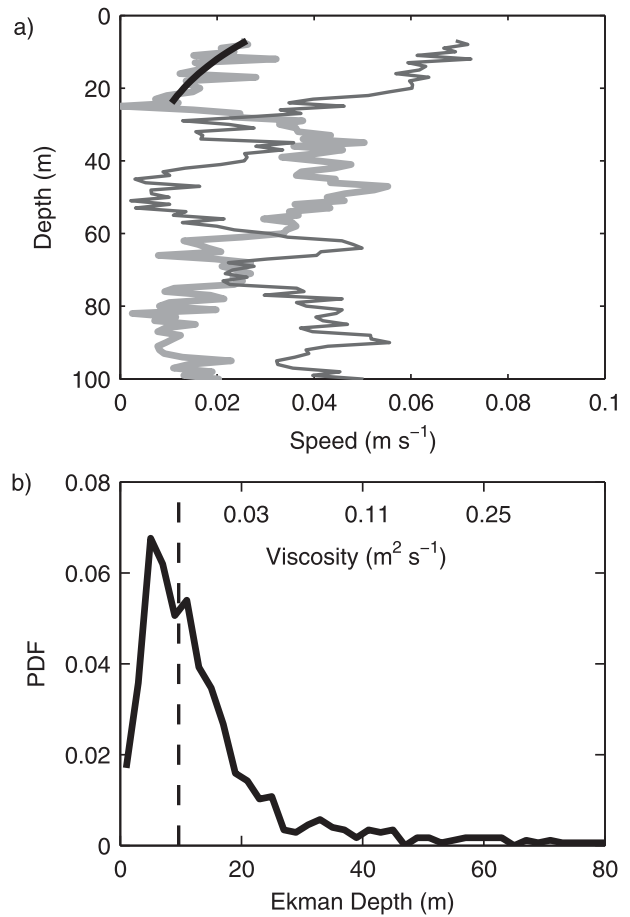


FIG. 5. Ekman depth estimates from (1). (a) Example profile on 22 Oct 2009 with an Ekman depth of 19 m. Total velocity magnitude (thin dark gray), Ekman velocity magnitude after removing the reference velocity (thick light gray), and the best-fit Ekman velocity magnitude (black) are shown. (b) Probability distribution function (PDF) of Ekman depth with corresponding viscosities indicated. Only the 90% of profiles for which the velocity magnitude decayed with depth are included. The median depth of 11 m (dashed) is shown.

### c. Heat flux parameterizations

A frequently used heat flux parameterization is based on the turbulent momentum flux and the deviation from the freezing temperature:

$$\langle \theta' w' \rangle = C_H u_* (\langle \theta \rangle - \theta_f), \quad (5)$$

where  $C_H$  is the heat transfer coefficient, and  $\theta_f$  is the freezing temperature (McPhee 1992; MCPhee et al. 2003). To evaluate the parameterization, heat flux and friction velocity at 6-m depth are considered. The freezing temperature is calculated using the mean pressure and salinity over each 40-min record. Because salinity affects the freezing temperature, salinity fluxes

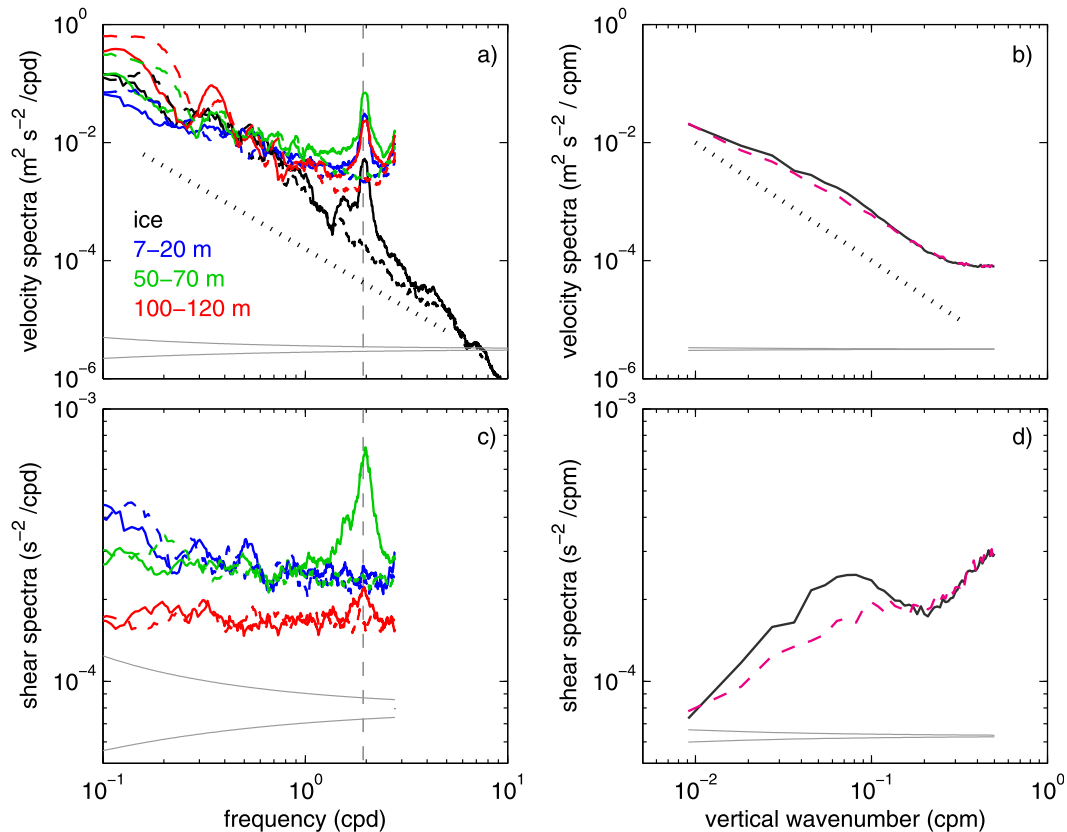


FIG. 6. Rotary spectra of (top) velocity and (bottom) velocity shear as a function of (a),(c) frequency and (b),(d) vertical wavenumber. Clockwise components are solid and counterclockwise components are dashed. As a function of frequency, spectra are calculated for ice velocity and for ocean velocity at each depth. Spectra are averaged over depths within the mixed layer (7–20 m), just below the mixed layer base (50–70 m), and deeper in the halocline (100–120 m). The dashed gray line shows a frequency of 12.42 h, which is the tidal period as well as the inertial period at 75°N. As a function of vertical wavenumber, spectra are calculated using the 40–150-m depth range and averaged over all profiles. Each profile is assumed to be an independent estimate. Gray curves show the 90% confidence interval with the number of degrees of freedom taken to be twice the record length, 173 days or 110 m, multiplied by the frequency or wavenumber. Dotted lines have a slope of  $-2$ .

can impact parameterized heat flux, and so heat and salt fluxes are jointly analyzed.

Observed heat flux was sometimes anticorrelated with observed salt flux, a feature that the parameterized heat flux lacks (Figs. 10a,b). When temperatures were near or below the freezing temperature, observed heat and salt fluxes were anticorrelated (Fig. 10a), while parameterized heat flux was near zero and uncorrelated with the observed salt flux (Fig. 10b). The observed heat flux versus salt flux scatterplot resembles the scatterplot for mean temperature and salinity, which is a straight line in winter with temperatures typically within  $0.01^{\circ}\text{C}$  of the freezing temperature (Fig. 10d). The slope of the freezing line in the  $\theta$ – $S$  scatterplot is identical to the slope in the heat flux versus salt flux scatterplot; heat and salt fluxes were anticorrelated in such a way that the turbulent fluxes did not alter  $\theta - \theta_f$ . This is consistent

with parameterizations that constrain salt flux so that  $\theta - \theta_f$  is not altered, which are valid when double diffusion is unimportant [see section 6.3 of McPhee (2008b) and see McPhee et al. (2008)].

The cause of correlated heat and salt fluxes can be deduced by examining temperature and salinity fluctuations over individual 40-min records as well as their nearest profiles. Two cases are considered: a positive heat flux and a negative heat flux (Fig. 11). In both cases, temperatures were below the freezing temperature with fluctuations of  $\theta$  and  $S$  that paralleled the freezing line (Figs. 11a,b). Correlated  $\theta$  and  $S$  fluctuations on time scales of seconds suggest that the upper portion of the water column consisted of water parcels with different  $\theta$  and  $S$ , all with the same deviation from the freezing temperature, which were vertically exchanged by turbulent motions. The nearest profiles of  $\theta$  and  $S$  support

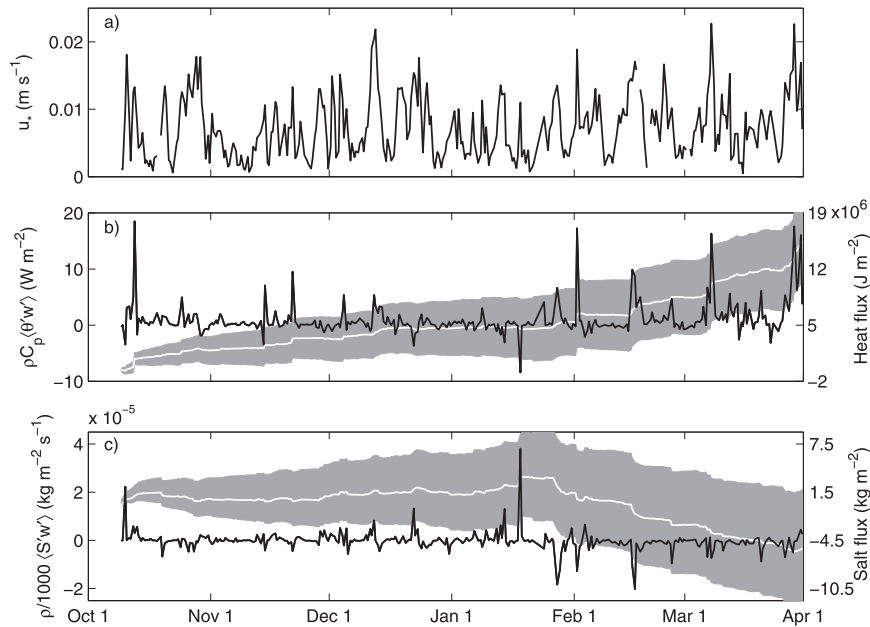


FIG. 7. Time series of (a) friction velocity [see (3)], (b) heat flux, and (c) salt flux. Positive heat/salt fluxes correspond to warm/salty water rising or cold/freshwater sinking. Cumulative turbulent fluxes with 95% confidence intervals (white lines and shading) are calculated assuming each 40-min estimate was representative of a 12-h period. Confidence intervals were estimated using a bootstrap procedure as the std dev of 10 000 cumulative flux estimates based on the observed values. The cumulative vertical heat and salt fluxes were  $16 \times 10^6 \pm 5 \times 10^6 \text{ J m}^{-2}$  and  $-5.5 \pm 7.0 \text{ kg m}^{-2}$ , respectively (mean  $\pm$  95% error).

this interpretation with near-uniform values of  $\theta - \theta_f$  in the upper 20–25 m, even though temperature (and salinity) varied with depth (Fig. 11c). The vertical gradients in temperature (and salinity) at 7–8-m depth were consistent with the signs of the observed fluxes as well (warmer water above colder water and a negative heat flux for 14 January; colder water above warmer water and a positive heat flux for 28 January). Water parcels with different  $\theta$  and  $S$  in the vertical but the same deviation from the freezing temperature may result from lateral fronts that tilt and restratify [see example fronts in Timmermans et al. (2012)].

Overall, the vertical exchange of water parcels with different  $\theta$  and  $S$  characteristics but the same deviation from the freezing temperature was occasionally influential. The effect of such events is shown using a modified heat flux parameterization:

$$\langle \theta' w' \rangle = C_H u_* (\langle \theta \rangle - \theta_f) + A_f \langle S' w' \rangle, \quad (6)$$

where  $A_f$  is the slope of the  $\theta$ – $S$  relation at the freezing temperature (Fig. 10c). The modified parameterization is simply (5) plus the heat flux required to maintain the same deviation from the freezing temperature for the observed salt flux. The modified parameterization correlates better with observed heat flux:  $r^2 = 0.8$  for the

modified parameterization (6), and  $r^2 = 0.7$  for the standard parameterization (5). Anticorrelated heat and salt fluxes were significant for a fraction of the heat flux events, and so the cumulative heat flux estimates agree to within error (95% confidence limits):  $16.0 \times 10^6 \pm 5.1 \times 10^6 \text{ J m}^{-2}$  for directly estimated heat flux,  $14.0 \times 10^6 \pm 4.0 \times 10^6 \text{ J m}^{-2}$  for parameterized heat flux (5), and  $15.3 \times 10^6 \pm 4.4 \times 10^6 \text{ J m}^{-2}$  for the modified parameterization (6). As individual flux observations and the collective 6-month record were constrained to the freezing temperature, this suggests that double diffusion was unimportant, which is consistent with other winter observations (McPhee et al. 2008), but not studies with melting ice (Notz et al. 2003) or with strong lateral fronts (McPhee et al. 2013). Finally, note that while it is difficult to observe salt flux, only occasionally correlated heat and salt fluxes support the conclusion that these salt flux observations are accurate (and are not affected by response time mismatches between temperature and conductivity sensors).

#### d. Momentum flux parameterizations

Numerical models rely on a relationship between velocity shear and turbulent momentum flux to parameterize momentum transfer between the ice and ocean. The most commonly used parameterization is a quadratic drag law:

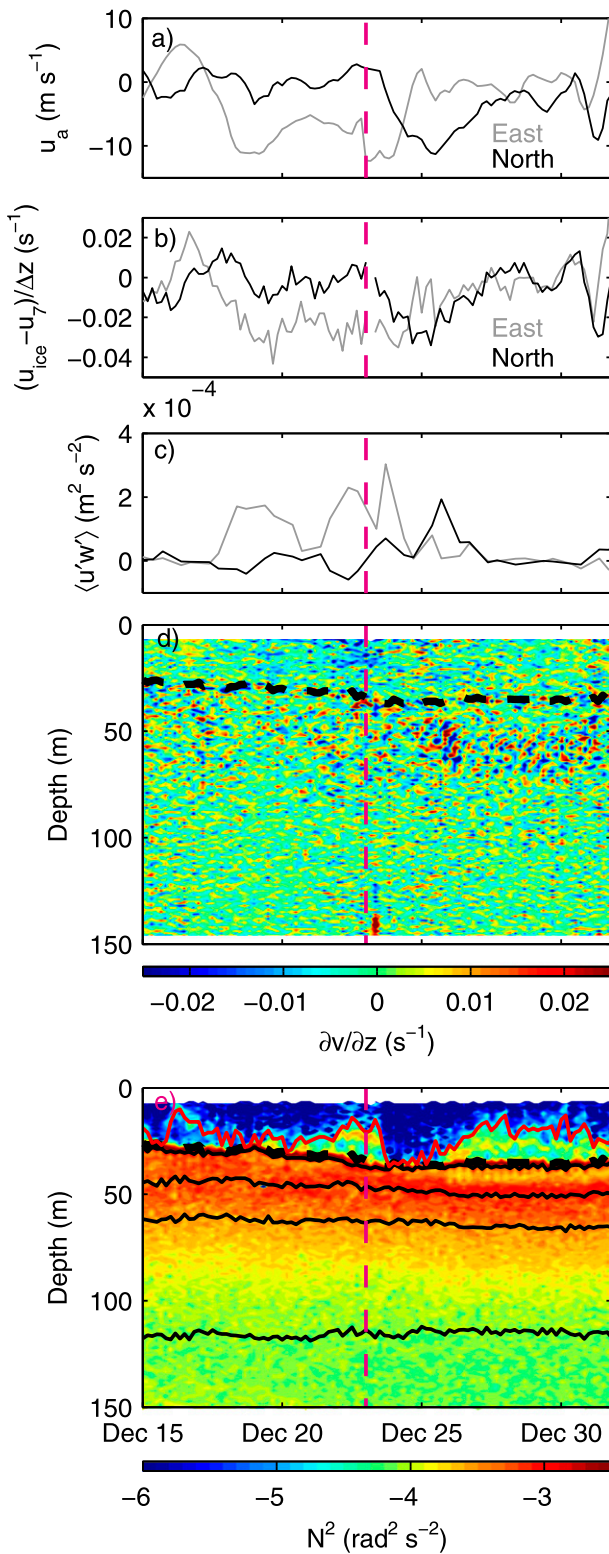


FIG. 8. Shear and stratification from 15 to 31 Dec. (a) Wind speed, (b) ice-ocean shear, (c) momentum flux, (d) vertical shear of northward velocity, and (e) stratification. The mixed layer base (dashed black), mixing layer base (red), and 23 Dec (dashed magenta) are shown. Isopycnals (solid black) as in Fig. 3.

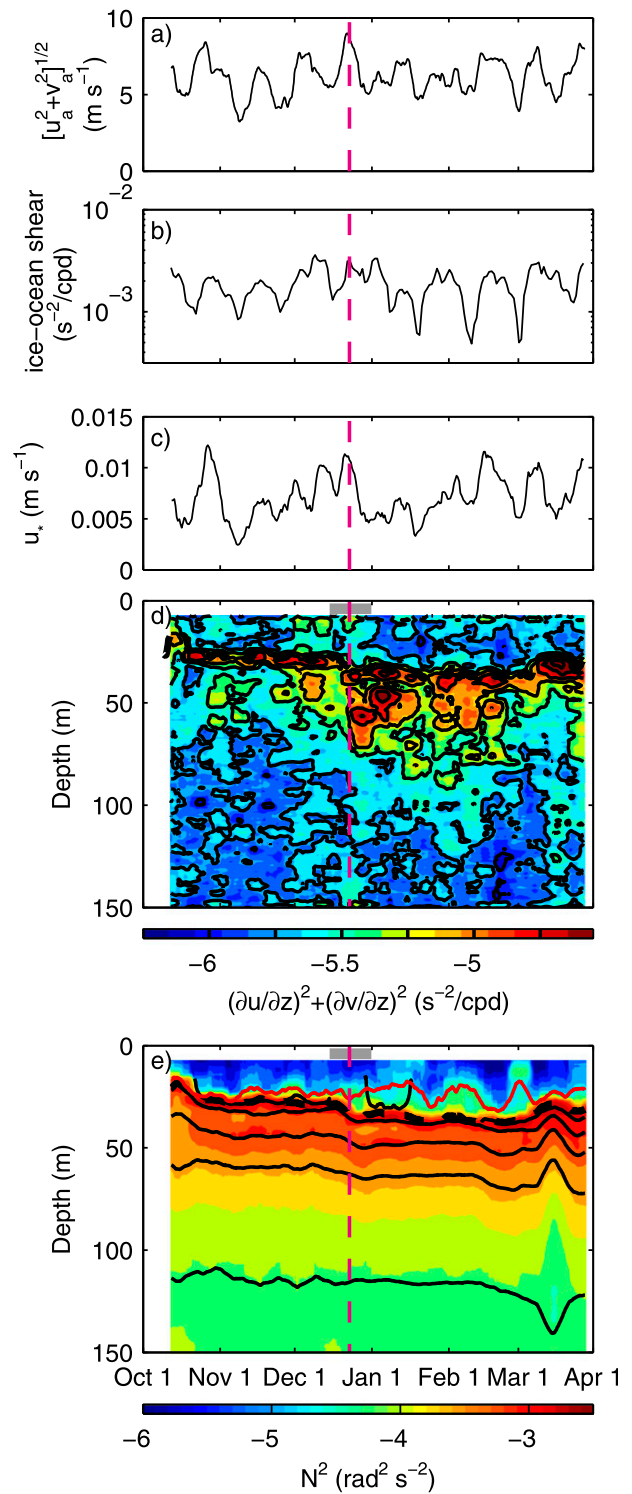


FIG. 9. Shear and stratification over the entire record. (a) Wind speed, (b) magnitude of ice-ocean shear, (c) momentum flux, (d) velocity shear, and (e) stratification. Ice-ocean shear and velocity shear are for 12.0–12.8-h periods only using a wavelet analysis. All records are smoothed over 7 days in time. Velocity shear and stratification are also smoothed over 5 m in depth. The gray line at 3-m depth in (d) and (e) indicates the time period shown in Fig. 8. Mixed layer base, mixing layer base, and 23 Dec as in Fig. 8. Isopycnals (black) as in Fig. 3.

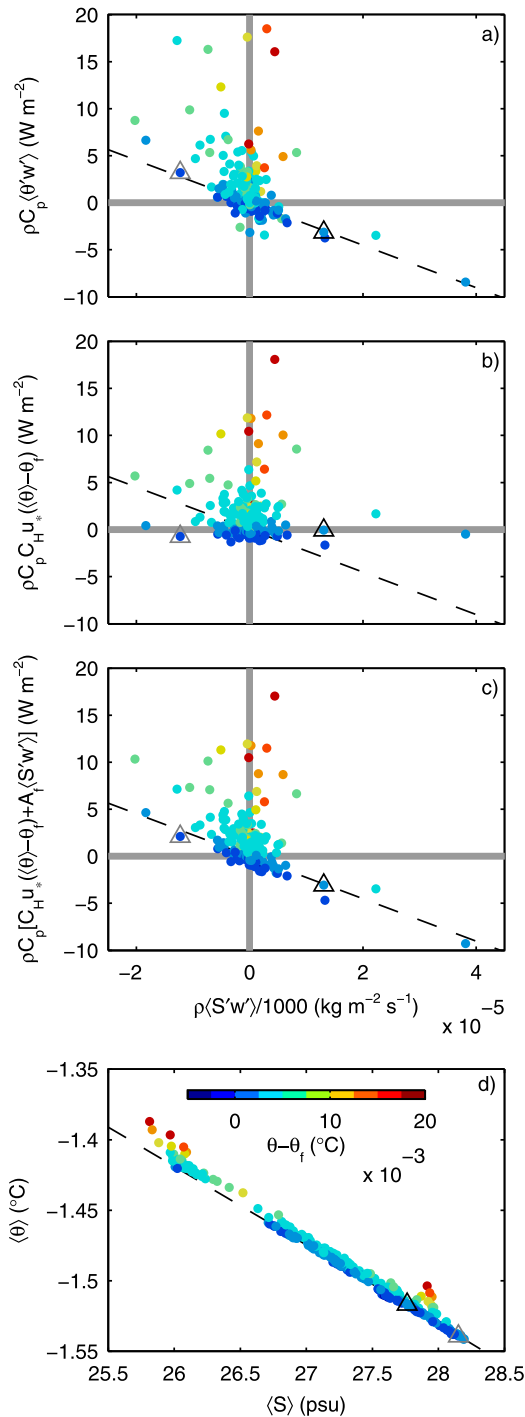


FIG. 10. (a) Directly observed heat flux, (b) parameterized heat flux, and (c) modified parameterized heat fluxes vs directly observed salt flux. (d) Mean  $\theta$  vs mean  $S$  at 6-m depth. A heat transfer coefficient of  $C_H = 0.0124$  is used because it gives the best agreement with directly observed heat flux. Colors indicate the deviation from the freezing temperature, which is calculated at the mean pressure of each 40-min sample. Dashed lines show the freezing temperature at the deployment mean pressure of 5.7 dbar in (d) and have the corresponding slope in (a)–(c). Black and gray triangles indicate values corresponding to the records shown in Fig. 11.

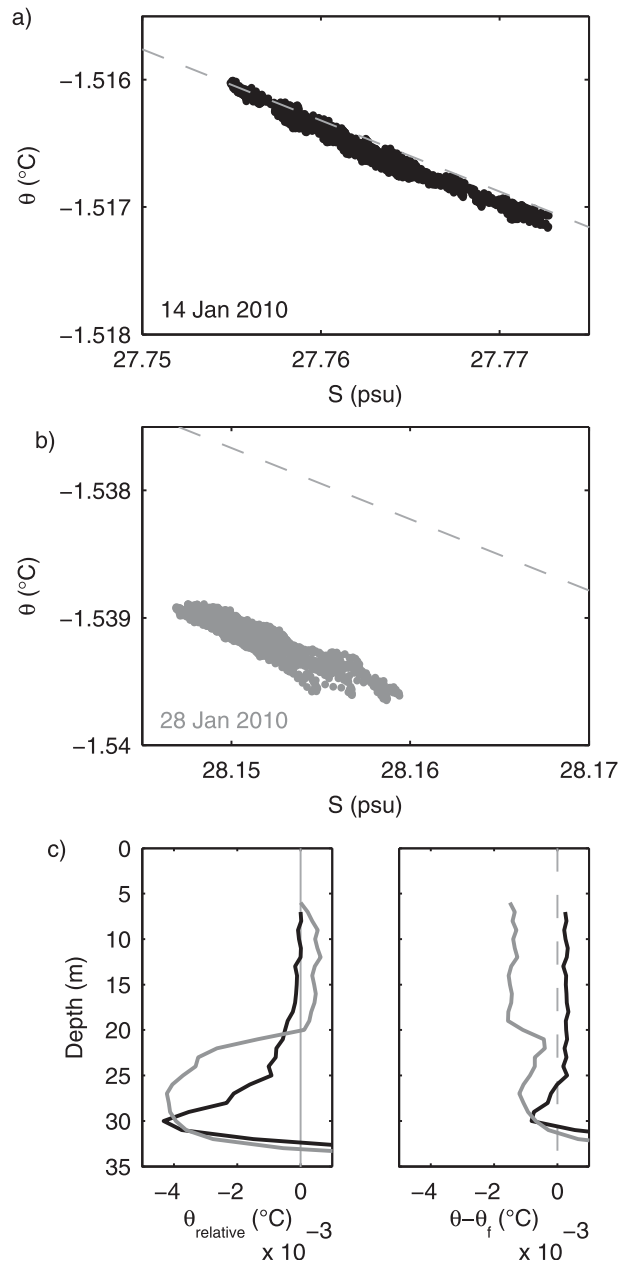


FIG. 11. Observed  $\theta$  vs  $S$  at 6-m depth from 45 min on (a) 14 Jan 2010 (fluctuations are shown in Fig. B1) and (b) 28 Jan 2010. Dashed lines show the freezing temperature at the sample mean pressure of 6.1 dbar in (a) and 5.5 dbar in (b). (c) Profiles of temperature relative to (left) the temperature at the shallowest depth and (right) the freezing temperature. Profiles were collected 1 h prior to the fluctuations at fixed depth.

$$\langle (v'w')^2 + (v'w')^2 \rangle^{1/2} = C_d [(u_{ice} - \langle u_6 \rangle)^2 + (v_{ice} - \langle v_6 \rangle)^2], \quad (7)$$

where  $C_d$ , the ice–ocean drag coefficient, is taken to be a constant, and we evaluate ice–ocean velocity shear using velocity from turbulent fluctuations at 6-m depth.

An alternative parameterization relies on a mixing length  $\lambda$ , which represents the distance over which dominant eddies diffuse momentum:

$$\langle (u'w'), (v'w') \rangle = -u_*\lambda \left( \frac{\partial u}{\partial z}, \frac{\partial v}{\partial z} \right), \quad (8)$$

where the velocity shear is the ocean shear at a particular depth. Three estimates of mixing length are considered based on observed parameters (the beginning of the inertial subrange  $k_{\max}$ , the turbulent dissipation rate  $\varepsilon_2$ , and Ekman diffusivity  $\kappa_E$ ):

$$\lambda_k = c_\lambda/k_{\max}, \quad (9a)$$

$$\lambda_\varepsilon = u_*^3/\varepsilon_2, \quad \text{and} \quad (9b)$$

$$\lambda_E = \kappa_E/u_*, \quad (9c)$$

where  $c_\lambda = 0.85$  (McPhee 1994), and  $\varepsilon_2$  is used as it agrees better with TKE production than when estimated using the inertial dissipation method [see section 3d(1)]. If (7) and (8) are valid, then the ice–ocean drag coefficient can be expressed as a mixing length:

$$\lambda_{C_d} = \sqrt{C_d} z_m \left( \frac{u_m/z_m}{u_l/z_l} \right), \quad (9d)$$

where  $u_l/z_l$  is the local ocean shear (e.g., that between 6- and 7-m depth), and  $u_m$  is the velocity difference associated with  $z_m$  (e.g., that between the ice and 6-m depth). Most comparisons of mixing length estimates are between (9a) and (9b) (e.g., MCPhee 1994), with order of magnitude comparisons to (9c) (e.g., MCPhee and Morison 2001); comparisons to estimates based on observed shear (9d) are rare. A third parameterization scheme is Rossby similarity theory, which utilizes the surface friction velocity  $u_{*0}$ :

$$u_{*0}^2 = \kappa \left\{ \frac{(u_{\text{ice}} - u_{\text{ref}})^2}{[\log(u_{*0}/fz_0) - A]^2} + \frac{(v_{\text{ice}} - v_{\text{ref}})^2}{[\log(u_{*0}/fz_0) - B]^2} \right\}, \quad (10)$$

where  $\kappa = 0.4$  is von Kármán's constant,  $z_0$  is a roughness length,  $A$  and  $B$  are constants, and the reference velocity is typically taken to be the geostrophic velocity of the ocean (McPhee 2012). Rossby similarity resembles (7) with an effective drag coefficient that depends on friction velocity. The remainder of this subsection first presents the turbulent dissipation rate, followed by the ice–ocean drag coefficient, and finally

comparisons of mixing length estimates (9a)–(9d) and momentum flux parameterizations (7), (8), and (10).

## 1) TURBULENT DISSIPATION RATE

The turbulent dissipation rate is estimated from horizontal wavenumber spectra (section 2c), which are first considered by averaging based on TKE production (section 2c). Three features of the average area-preserving spectra  $kE(k)$  stand out (Fig. 12c): 1) at all levels of TKE production, the observations extend into an inertial subrange with a slope of  $-2/3$  [ $E(k)$  has a slope of  $-5/3$ ]; 2) average spectral levels, and so estimates of dissipation, scale with TKE production; and 3) the wavenumber corresponding to the maximum in the area-preserving spectra scales with TKE production only for the vertical component, as in MCPhee (2004). Average spectra are not consistent with isotropic turbulence, in which along-stream and vertical spectral levels are larger than across-stream spectral levels by a factor of 4/3; vertical spectral levels in particular were not elevated above along-stream spectral levels. While additional observations are desirable to reduce noise in the average spectra, such a situation may indicate anisotropic velocity fluctuations or may result because of the effects of underice ridges, as has been previously observed (McPhee 2004).

The turbulent dissipation rate can be adequately estimated from a fit to a  $-5/3$  power law [e.g., (4a),  $\varepsilon_1$ , and Fig. 12a] or based on a single point in the inertial subrange [e.g., (4b),  $\varepsilon_2$ , and Fig. 12b]. The two dissipation rate estimates were correlated with  $r^2 = 0.8$  (Fig. 12d) and similar to previous estimates (McPhee 1994; MCPhee and Stanton 1996; MCPhee 2002, 2004; Fer and Sundfjord 2007; Sirevaag et al. 2011). Dissipation was also correlated with but slightly smaller than TKE production (Fig. 12e). Dissipation estimated from a single point in the inertial subrange ( $\varepsilon_2$ ) was correlated better with TKE production than when directly estimated from a  $-5/3$  slope ( $\varepsilon_1$ ). The conversion to/from potential energy  $-(g/\rho)\langle \rho'w' \rangle$ , which is equivalent to the buoyancy flux, was typically more than an order of magnitude smaller than either production or dissipation (Fig. 12e) and so negligible in the TKE equation. The majority of TKE produced by ice–ocean shear was dissipated locally within the mixed layer.

## 2) ICE–OCEAN DRAG AND HYDRAULIC ROUGHNESS

Constant as well as time-varying drag coefficients are considered. Over the entire 6 months of observations a best fit to (7) is obtained with  $C_d = 7.1 \times 10^{-3}$  ( $r^2 = 0.69$ ). A time-varying drag coefficient is considered by applying (7) to each flux measurement individually. The

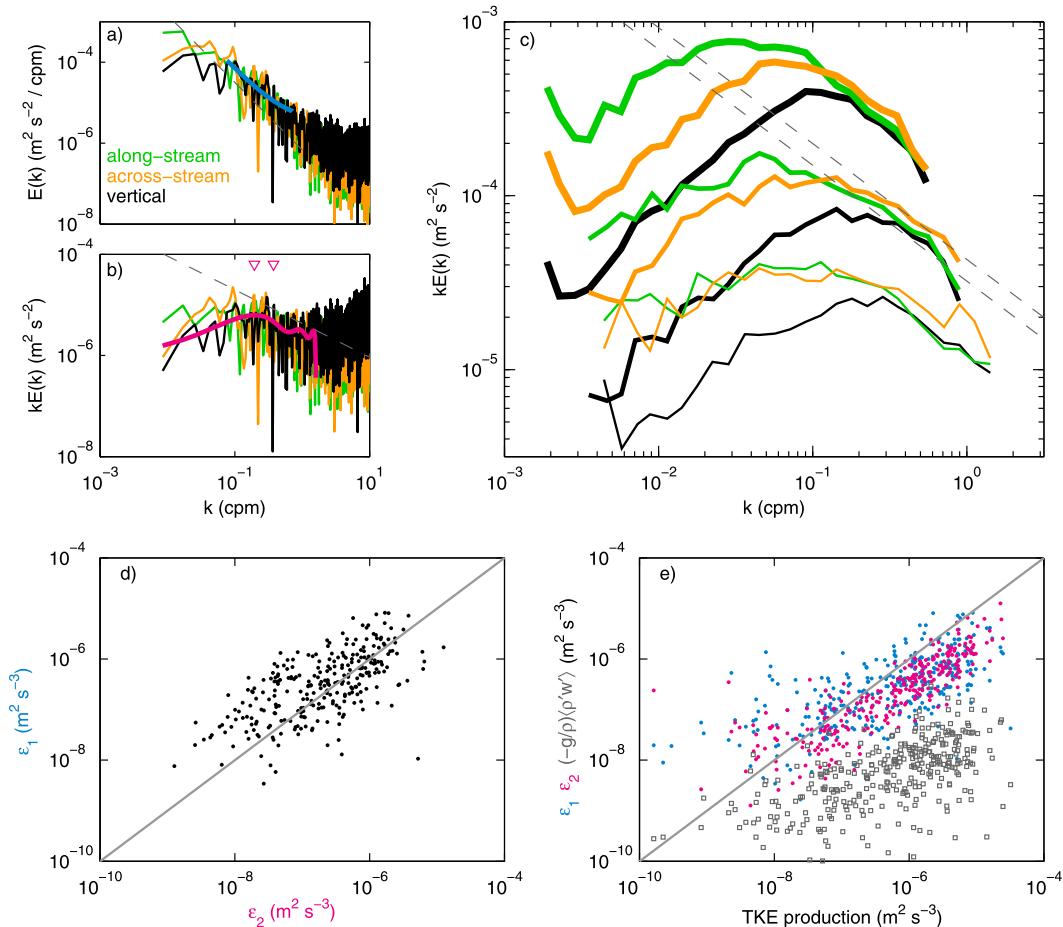


FIG. 12. Turbulent dissipation rate. Example velocity spectra on 7 Nov 2009 showing (a) the best fit of a  $-5/3$  slope to the vertical velocity spectra used to estimate  $\varepsilon_1$  (blue) and (b) the polynomial fit to the area-preserving vertical velocity spectra (magenta). Triangles show the peak wavenumber and wavenumber used to estimate  $\varepsilon_2$ . Dashed gray lines have a slope of  $-5/3$  in (a) and  $-2/3$  in (b). (c) Area-preserving velocity spectra averaged according to the production of turbulent kinetic energy: less than  $10^{-7} \text{ m}^2 \text{ s}^{-3}$  (thin lines), from  $10^{-7}$  to  $10^{-6} \text{ m}^2 \text{ s}^{-3}$  (medium lines), and greater than  $10^{-6} \text{ m}^2 \text{ s}^{-3}$  (thick lines). Dashed gray lines have a slope of  $-2/3$  and are vertically offset by  $4/3$ . (d) Comparison of the two estimates of turbulent dissipation rate. (e) Turbulent dissipation rate ( $\varepsilon_1$  in blue and  $\varepsilon_2$  in magenta) and buoyancy flux magnitude (gray squares) vs TKE production.

derived drag coefficient varied by more than an order of magnitude, from values smaller than  $1 \times 10^{-3}$  to greater than  $10 \times 10^{-3}$ , with a median value of  $10.1 \times 10^{-3}$  (Fig. 13a). Such values have been previously observed [see summary tables in Shirasawa and Ingram (1991) and Lu et al. (2011)], with variations attributed to differences in underice topography and rough ice resulting in a larger drag coefficient. Although the ITP was moored in the same ice floe over the entire 6 months, the underice topography may have changed because of the ice growth or ridging events. The largest drag coefficients were primarily observed during straight drift segments toward the west and southwest (Fig. 13c), suggesting that the ice floe drift was approximately irrotational, the underice topography was linearly ridged, and the drag coefficient

varied because of the changes in the direction of the ice–ocean shear relative to the orientation of these ridge features. The drag coefficient tended to be larger for two directions of the ice–ocean shear roughly  $180^\circ$  apart (Fig. 13b), supporting this hypothesis.

A roughness length scale is estimated and is advantageous because it is independent of measurement depth. Within a logarithmic boundary layer, the roughness length is related to the drag coefficient by  $\kappa^{-1}(u_* / u_{*0}) \log(z_m / z_0) = C_d^{-1/2}$ . To estimate the roughness length, assumptions are made regarding 1) the depth of the ice–ocean interface, which is only known at the beginning of the deployment, and 2) the surface friction velocity. The estimated depth of the logarithmic boundary layer is 0.25–2.0 m (section 3a), smaller than  $z_m = 3.4$  m;

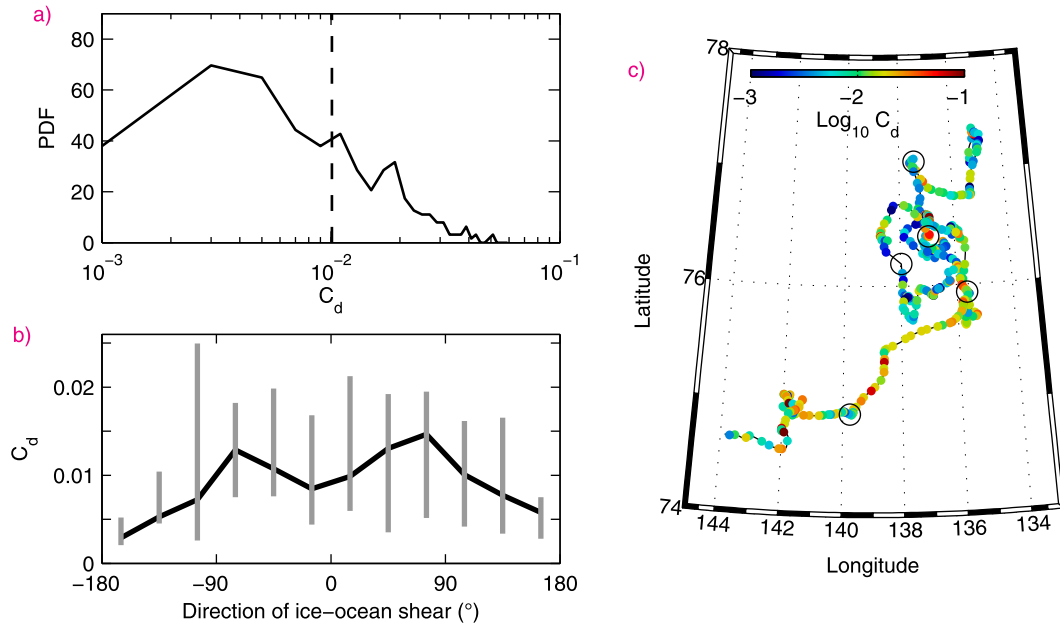


FIG. 13. Ice–ocean drag coefficient. (a) PDF of  $C_d$  from each 40-min record. Dashed line shows the median value of  $10.1 \times 10^{-3}$ . (b) The ice–ocean drag coefficient vs the direction of ice–ocean shear. Black line shows the median value in each direction bin, with vertical lines connecting the 25th and 75th percentile values. (c) The ice–ocean drag coefficient along the drift track. Black circles show 1 Nov, 1 Dec, 1 Jan, 1 Feb, and 1 Mar.

the roughness length scale is most likely overestimated if our observations are not within the logarithmic boundary layer. An upper bound of  $z_0 = 6.4$  cm results using the median drag coefficient of  $10.1 \times 10^{-3}$ ,  $z_m = 3.4$  m, and  $u_{*0}/u_* = 1$ . Ice growth of 70 cm during winter would reduce the estimated  $z_0$  to 5.0 cm. A surface friction velocity corresponding to  $u_{*0}/u_* = 1.23$  (the median value using Ekman depth to describe the decay of  $u_*$  with depth) would reduce  $z_0$  to 2.5 cm. Such estimates are again consistent with previous observations of multiyear ice (McPhee 2012, and references therein).

### 3) MIXING LENGTH

Mixing length has been found to depend on the smallest of three length scales (McPhee 1994; MCPhee and Morison 2001; MCPhee 2008a; Sirevaag et al. 2010): the geometric scale of the logarithmic boundary layer  $\kappa z_m$ ; the planetary scale  $\Lambda_* u_*/f$ , with  $\Lambda_* = 0.028$  as in MCPhee (2008a); and the Obukhov length scale  $u_*^3/\kappa \langle b'w' \rangle$ , where  $\langle b'w' \rangle$  is the buoyancy flux. The geometric length scale was initially 1.4 m and may have decreased throughout the deployment because of ice growth. The Obukhov length scale is too large to be important, with only 5% of values less than 5 m, reflecting the weak buoyancy forcing of these observations (Fig. 12e). For negligible buoyancy flux,

$$\lambda = \begin{cases} \Lambda_* u_*/f & \text{for } \Lambda_* u_*/f < \kappa z_m \\ \kappa z_m & \text{for } \Lambda_* u_*/f > \kappa z_m \end{cases} \quad (11)$$

Note that the mixing length depends on  $u_*$  for a range of  $u_*$ ; that range depends on the distance from the boundary. The planetary scale was less than the maximum geometric scale for  $u_* < 0.007 \text{ m s}^{-1}$ , which corresponded to 54% of observations.

Three of the four estimates of mixing length [(9a)–(9d)] agreed well with (11). Mixing length based on  $k_{\max}$  [(9a)] and based on  $C_d$  [(9d)] was almost always smaller than the geometric length scale and scaled with the planetary scale (Figs. 14a,d). This is similar to mixing length estimates based on  $k_{\max}$  from previous observations (McPhee 2008a, his Fig. 13; Sirevaag et al. 2010, their Fig. 6). The shear factor in (9d) of  $(u_m/z_m)/(u_l/z_l) = 3$  was chosen so that derived mixing lengths would agree in magnitude with mixing length based on  $k_{\max}$ . Had observations of velocity at 7-m depth been available simultaneously with those at 6-m depth, this factor could have been directly determined; the factor of 3 is consistent with the shear between the ice and ocean exceeding the shear at any specific depth within the Ekman layer. As  $\lambda C_d \propto C_d^{1/2}$ , the drag coefficient itself scaled with the planetary and geometric scales; a drag coefficient that depends on  $u_*$  is consistent with Rossby similarity. Mixing length based on the turbulent dissipation

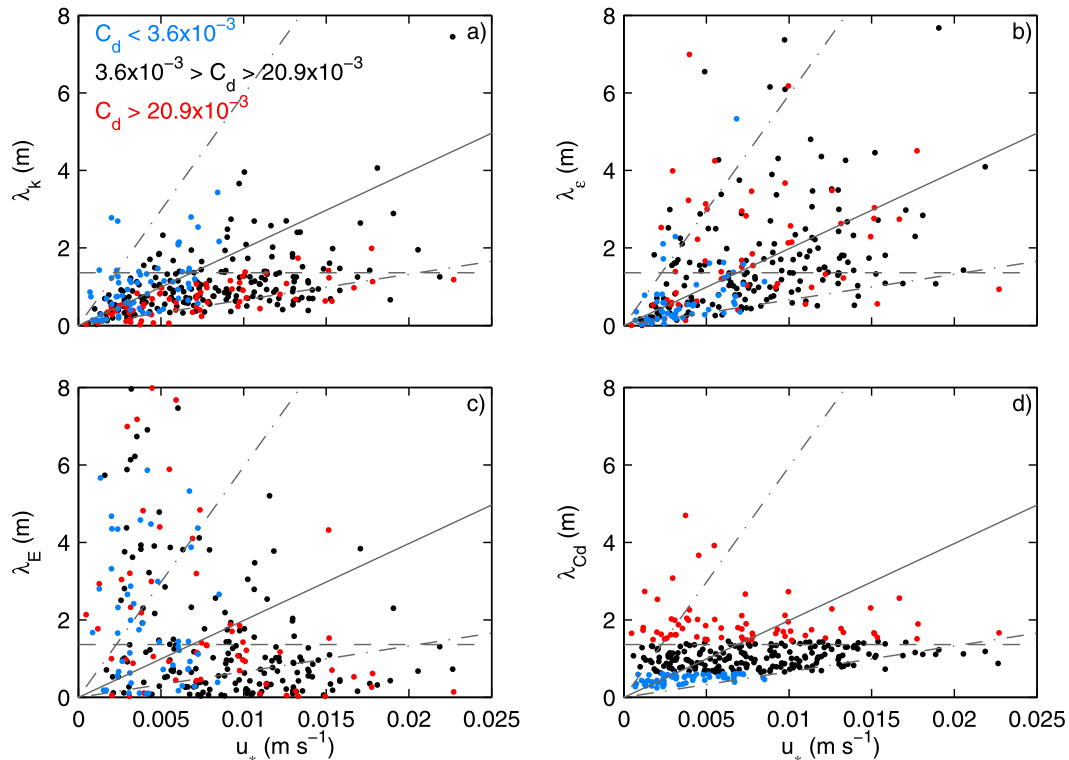


FIG. 14. Mixing length estimates vs friction velocity. Mixing length is estimated from (a) the beginning of the inertial subrange  $k_{\max}$ , (b) the turbulent dissipation rate  $\varepsilon_2$ , (c) Ekman viscosity using viscosities that correspond to Ekman depths of 0–50 m linearly interpolated to the times of flux measurements, and (d) the ice–ocean drag coefficient. Color indicates the largest (red) and smallest (blue) 20% of drag coefficients. Horizontal dashed lines correspond to the geometric scale  $\kappa z_m$ . Gray lines show the planetary scale  $\Lambda_* u_* l_f$  (solid) and the planetary scale multiplied by factors of 3 and  $1/3$  (dashed–dotted), with  $\Lambda_* = 0.028$ .

rate (9b) was similar, but had 37% of mixing lengths larger than the geometric scale (Fig. 14b). Mixing length based on Ekman viscosity did not scale with the geometric or planetary scales (Fig. 14c) and approximately decreased with increasing  $u_*$ . Ekman viscosity was more representative of mixing over a larger depth range than specifically at 6-m depth, suggesting that viscosity varied with depth. Overall, the most appropriate mixing length or drag coefficient increases with  $u_*$  at small  $u_*$  and is best estimated from a variable ice–ocean drag coefficient or the beginning of the inertial subrange.

Mixing length estimates had significant scatter about the planetary and geometric scales and did not correlate with each other. Considering the largest and smallest 20% of drag coefficients illustrates that each estimate is independent; large drag coefficients corresponded to  $\lambda_{C_d}$  larger than the geometric scale (Fig. 14d) and  $\lambda_k$  smaller than the planetary scale (Fig. 14a), while  $\lambda_\varepsilon$  and  $\lambda_E$  (Figs. 14b and 14c) did not show a relationship to the drag coefficient. With the exception of  $\lambda_E$ , scatter in mixing length was largely confined to a region within a factor of 3 of the planetary scale. Scatter about the planetary scale

for  $\lambda_k$  was related to the drag coefficient; elevated drag coefficients, which correspond to weak velocity shear for a given momentum flux, corresponded to an inertial subrange that began at smaller horizontal scales and mixing lengths that were smaller than the planetary scale. It is unclear what caused scatter in the other mixing length estimates; there was no clear relationship to other parameters including buoyancy flux, mixed layer depth, or mixing layer depth. Variations in  $\Lambda_*$ ,  $c_\lambda$ , and the ratio of the ice–ocean shear to local ocean shear are possible, as are influences of the inferred linear ridge structure of the underice topography or other sources and sinks of momentum such as the internal wave field. The significant scatter in mixing length about the planetary scale and tendency for the mixing length to be less than the geometric scale was robust between estimates.

#### 4) MOMENTUM FLUX VERSUS VELOCITY SHEAR

Momentum flux parameterizations [(7), (8), and (10)] are compared by considering the relationship between momentum flux and velocity shear (Fig. 15). The direction of momentum flux aligned with that of the ice–ocean

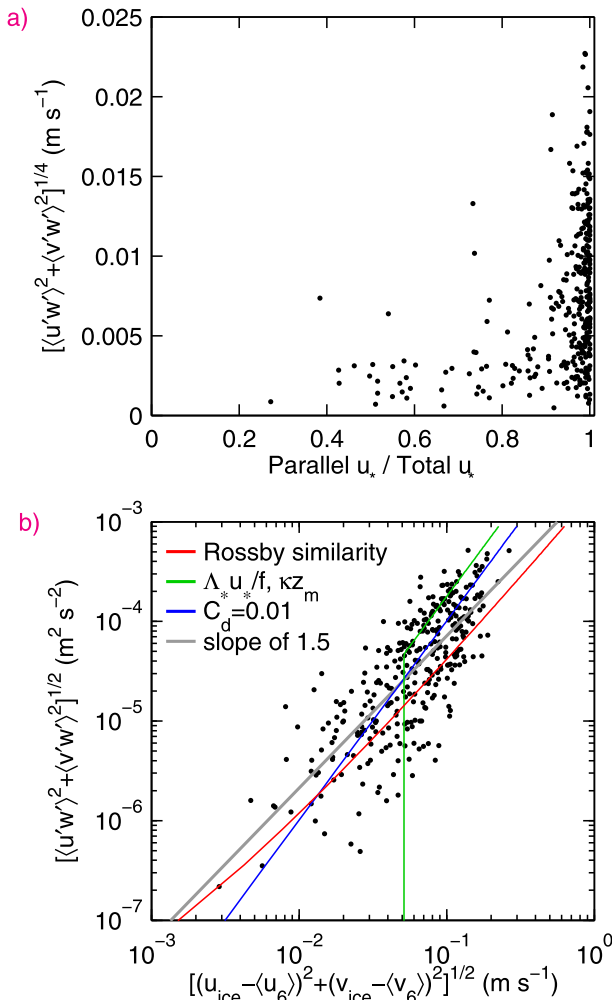


FIG. 15. (a) Fraction of momentum flux at 6-m depth directed parallel to the ice-ocean velocity difference. (b) Scatterplot of momentum flux at 6-m depth vs the ice-ocean velocity difference. Theoretical predictions based on Rossby similarity with  $z_0 = 6.2$  cm,  $A = 2.1$ ,  $B = 2.3$  (red), the planetary and geometric scales (green), and a constant drag coefficient of  $10.1 \times 10^{-3}$  (blue) are shown. The best-fit slope of 1.5 (gray) is also shown.

velocity difference as predicted by (7), with perpendicular momentum flux most common for the smallest values of  $u_*$  (Fig. 15a). In magnitude, a constant drag coefficient [(7)] corresponds to a slope of 2 between  $u_*^2$  and velocity shear, Rossby similarity [(10)] corresponds to a smaller slope, and the geometric and planetary scales [(11)] converted into a drag coefficient using (9d) result in a constant value of shear at low  $u_*$  and a slope of 2 at high  $u_*$ . Using realistic values for the ice-ocean system [ $C_d = 10.1 \times 10^{-3}$ ,  $z_0 = 6.4$  cm, and  $u_{*0}/u_* = 1$ , as in section 3d(2);  $A = 2.1$  and  $B = 2.3$  as in SHEBA and typical of the Arctic ice-ocean system (McPhee 2008b, chapter 9; MCPhee 2012)], scatter in the observations was greater than the differences between

parameterization schemes (Fig. 15b). Disagreement with the planetary scale at small  $u_*$  may have resulted from assuming a constant ratio of ice-ocean shear to local shear in (9d) and does not indicate that mixing length is an invalid approach. The best-fit relationship to the observed  $u_*^2$  and velocity shear was significantly different from the quadratic with a slope of  $1.53 \pm 0.14$ , similar to the Rossby similarity solution and previous observations that also support a slope less than 2 (McPhee 1979, 2012). For large friction velocities, scatter in the observations decreased and the slope became closer to a value of 2. The three approaches to parameterizing momentum flux considered here adequately captured the relationship between turbulent fluctuations and velocity shear (the observed versus predicted ice-ocean velocity difference corresponds to  $r^2 = 0.78$  for Rossby similarity,  $r^2 = 0.79$  for a constant drag coefficient, and  $r^2 = 0.81$  for mixing length based on the planetary and geometric scales).

#### 4. Summary and conclusions

A diverse collection of processes on a range of spatial and temporal scales were observed with the ITP-V. These included velocity observations 1) from just below the ice-ocean interface to well below the mixed layer base at high enough frequency to observe internal waves, and 2) while at fixed depth allowing vertical fluxes of heat, salt, and momentum and the turbulent dissipation rate to be quantified. Sampling over a period of 6 months provided not just a single observation, but robust statistics following the temporal evolution of the ice-ocean system. Key findings include the following:

- 1) Increased internal wave activity is associated with changes to stratification within the surface mixed layer and turbulent fluxes of heat and salt just below the ice-ocean interface (section 3b).
- 2) Anticorrelated heat and salt fluxes resulted from turbulent mixing of water with different  $\theta$  and  $S$  but the same deviation from the freezing temperature (section 3c).
- 3) Velocity near the ice-ocean interface is adequately described using a constant drag coefficient, mixing length, or Rossby similarity approach, while Ekman viscosity describes velocity near the base of the mixing layer; mixing length is best estimated from the horizontal wavenumber of the beginning of the inertial subrange or a variable drag coefficient and increases with friction velocity up to the geometric scale (section 3d).

Because of the unsteady nature of the Arctic ice-ocean system, with winds and ice velocity that vary on scales of

hours to many days or longer, specific parameters (e.g., the turbulent dissipation rate, heat flux, salt flux, Ekman viscosity, and internal wave energy levels) typically have a wide range of observed values. The specific parameters observed here are consistent with this wide range of observed values and have provided an excellent dataset for evaluating turbulent processes and their parameterizations in the ice–ocean system.

Within the mixed layer, the velocity structure largely consisted of Ekman veering and near-inertial/tidal motions. Despite the significant temporal variability at the inertial and tidal time scales, Ekman veering was evident in most profiles with ocean currents that veered toward the right and decayed with depth. The ice cover suppressed many other processes, such as surface waves, making Ekman veering a dominant feature of the surface circulation.

The internal wave field is best characterized as having a slight preference for downward propagation with internal waves occasionally locally generated in the mixed layer or at the mixed layer base. Vertical mixing associated with increased internal wave activity impacted stratification within the mixed layer as well as heat and salt fluxes near the ice–ocean interface; entrainment likely occurred at the base of the shallow mixing layers. A clear signal of internal waves affecting the momentum balance was not evident; momentum transferred to the internal wave field should reduce the momentum transferred to mixed layer ocean currents and subsequently elevate the ice–ocean drag coefficient (and decrease the hydraulic roughness; e.g., Morison et al. 1987; McPhee and Kantha 1989). Both the internal wave field and ice–ocean drag coefficient varied significantly in time.

Heat and salt fluxes were sometimes anticorrelated because of the vertical exchange of water parcels with different  $\theta$  and  $S$  but the same deviation from the freezing temperature, which was most likely to occur when the water parcels were closest to the freezing temperature. Previous studies also document anticorrelated heat and salt fluxes [e.g., compare Figs. 8 and 11 of McPhee (2008a)] and suggest this results when double diffusion is unimportant (McPhee et al. 2008). It is not clear if correlated heat and salt fluxes were associated with any particular process such as brine rejection when the mixed layer was near the freezing temperature or weak and shallow turbulent mixing that did not reach to the base of the mixing layer. Investigating any differences in turbulent eddy structure between processes, such as brine rejection events and vertical entrainment events, or between eddies primarily resulting in large salt fluxes, versus large heat fluxes, is beyond the scope of the present paper.

These observations allow several momentum flux parameterization schemes and mixing length estimates to be evaluated. A wider range of friction velocities has been considered than with previous studies; an even wider range of friction velocity may be needed to distinguish between momentum flux parameterization schemes. Constant drag coefficients, mixing length based on the planetary and geometric scales, and Rossby similarity theory were all valid approaches to parameterizing momentum flux. Ekman diffusivity was most representative of velocity shear over the larger distance between the ice and base of the mixing layer. Mixing length estimates had significant scatter about the planetary scale, with the cause of such scatter unclear and different between mixing length estimates. Considering the ice–ocean drag coefficient in a mixing length framework shows that the dependence of the drag coefficient on friction velocity is partly a manifestation of the influence of the planetary scale on the mixing length. Note that these observations correspond to a single point along the ice floe. An ITP-V near different ice topography may yield different momentum fluxes and relevant parameters (e.g.,  $C_d$ ,  $z_0$ , and  $\lambda$ ); it is unlikely that the full range of parameter space has been explored.

Several open questions remain, especially with respect to a changing Arctic ice–ocean system. As sea ice thins and presumably accelerates in the Arctic, ensuring a correct parameterization scheme for momentum in particular is essential. Stratification and shallow mixing layers affect Ekman veering and upper-ocean velocity as well; changes to upper-ocean stratification will impact ocean circulation in the Arctic. Anticyclonic eddies, for which absolute velocity observations are not commonly obtained, impact the distribution of tracers between the boundary and interior regions; a larger collection of observations is needed to address their impact on the Arctic Ocean. Finally, we note that these observations have focused on the winter season and fully ice-covered conditions. Observations that span an entire year will show how the ice–ocean system evolves seasonally and responds to decreased ice cover in summer.

*Acknowledgments.* We thank two anonymous reviewers for suggestions that improved this manuscript. Support for this study and the overall ITP program was provided by the National Science Foundation and Woods Hole Oceanographic Institution. Support for S. Cole was partially through the Postdoctoral Scholar Program at the Woods Hole Oceanographic Institution, with funding provided by the Devonshire Foundation. We gratefully acknowledge the crew of the CCGS *Louis S. St-Laurent* for support with deployment and recovery of this ITP-V. NCEP reanalysis data from the NOAA/OAR/ESRL

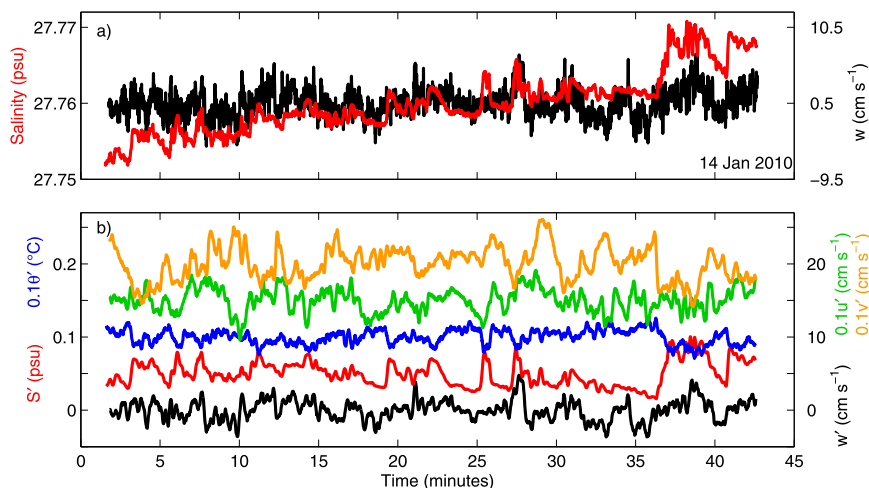


FIG. B1. Fixed-depth observations at 6-m depth on 14 Jan 2010. (a) The 1-s records of salinity and vertical velocity. (b) Fluctuations of vertical velocity, salinity, temperature, and horizontal velocity offset vertically. Fluctuations are the 1-s records averaged to a 10-s record and then detrended.

PSD, Boulder, Colorado, were obtained from their website (<http://www.esrl.noaa.gov/psd/>).

## APPENDIX A

### Derivation of Ocean Velocity

Several calibrations are employed to obtain an accurate estimate of ocean velocity from ITP-V sensor observations. Details of the Nobska Inc. modular acoustic velocity sensor (MAVS; [www.nobska.net](http://www.nobska.net)) can be found in Thwaites and Williams (1996), Williams et al. (2010), and Thwaites et al. (2011). Relative velocity past the sensor  $u_{\text{rel}}$  is derived from an acoustic travel time calculation as  $u_{\text{rel}} = c^2 \Delta t / 2d$ , where  $c$  is sound speed,  $\Delta t$  is a travel time difference, and  $d$  is the acoustic pathlength. Sound speed is derived from observed temperature, salinity, and pressure. Time-invariant errors in pathlength and travel time are accounted for using a magnitude correction that all velocity components are multiplied by. The heading is calculated from the three-axis fluxgate compass after biases of 0.0094 and 0.0102 for the  $x$  and  $y$  components are applied. These biases were determined from a subset of the observations where the wire angle was less than  $0.75^{\circ}$ . The local magnetic declination as well as a preliminary heading bias of  $13^{\circ}$ , determined from a laboratory “compass spin” prior to deployment, are also accounted for. A final heading bias as well as biases in pitch and roll are applied to account for any difference in the orientation of the motion sensors and the velocity sensor as well as any remaining bias in the heading. The magnitude

correction, as well as pitch, roll, and heading biases are determined so that the ice velocity is most completely removed from the relative velocity; for zero absolute ocean velocity, the relative velocity measured by the sensor will be equal and opposite to the ice velocity. Values of 1.2 for the magnitude correction,  $3.5^{\circ}$  for pitch bias,  $-1^{\circ}$  for roll bias, and  $-12^{\circ}$  for heading bias were inferred from the preliminary data and used in creating the final velocity estimates.

Once the above calibrations are applied, the velocity due to the motion of the profiler along the wire and ice velocity are accounted for. A profiler moving along a nonvertical wire will observe a relative velocity in the horizontal as well as vertical directions in the absence of any ice or ocean flow. This velocity is removed before the relative velocity measured by the sensors is rotated into a geographic east–north–up coordinate system. All three components of this velocity are estimated using  $\partial Z / \partial t$  derived from pressure as measured by the CTD, together with the pitch, roll, and heading of the ITP-V. To avoid introducing high-frequency noise, pitch, roll, and heading are smoothed as in Williams et al. (2010). Absolute velocity for the parked measurements was calculated without subtracting out the motion of the profiler using a  $\partial P / \partial t$  estimate because the profiler was at a fixed depth at these times. Ice velocity is assumed to be constant during the duration of each profile and each fixed-depth measurement. Ice velocity is interpolated in time to the beginning of each down profile, the end of each up profile, and the mean time of each fixed-depth profile; this ensures the best estimate of shear between the ice and upper-ocean currents.

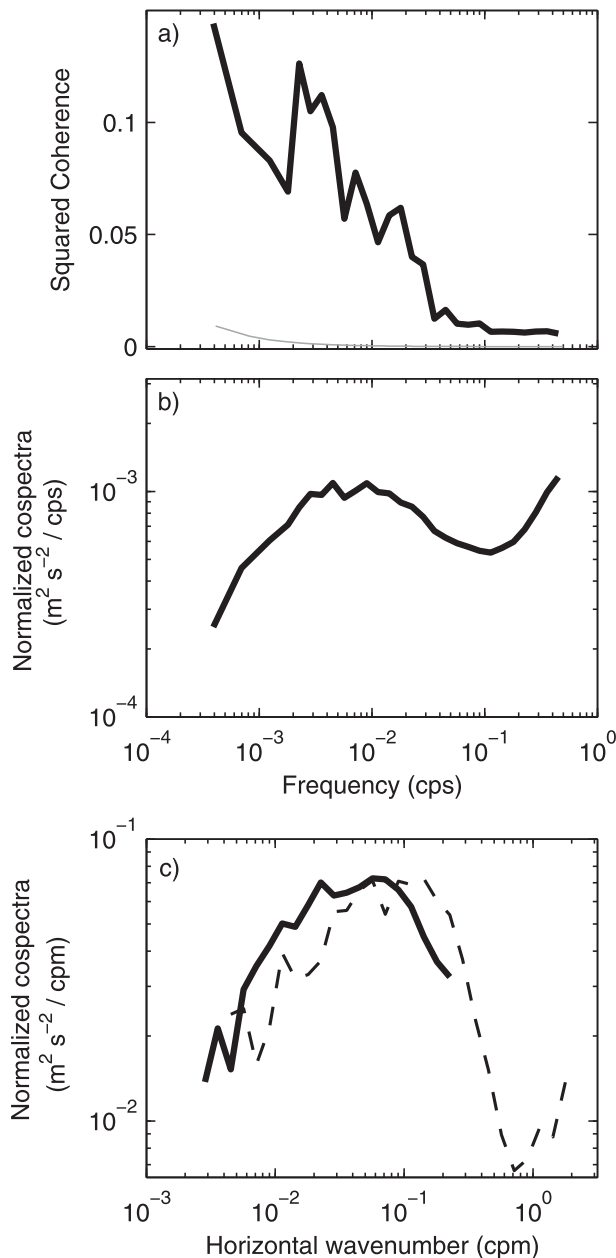


FIG. B2. Statistics of fixed-depth observations. (a) Squared coherence of  $u$  and  $w$  in frequency space averaged over all observations. The 95% confidence limit is shown (gray). Normalized cospectra of  $u$  and  $w$  in (b) frequency space averaged over all observations and (c) horizontal wavenumber space averaged over relative velocities greater than  $0.069 \text{ m s}^{-1}$  (solid) and less than  $0.069 \text{ m s}^{-1}$  (dashed). Cospectra are normalized so that the area under the curve is equivalent to the covariance.

The velocity and CTD sensors on the ITP-V do not start or stop logging at precisely the same time, nor do they necessarily sample at exactly the same rate. Thus, a scheme is required to align the two data series and map them to a common time base. For profile sampling, the

sensors log data for 2 min before initiating each profile and 2 min after stopping each profile; alignment is achieved by matching the start and stop transients in  $\partial P/\partial t$  and  $w$ . A lag of 12.0 s was derived between the start of the CTD data records and the start of the velocity sensor data; this time offset was applied to the profile data as well as the fixed-depth observations. A sample rate factor of 0.500 s was also derived and reflects the factor of 2 differences between the manufacturer-specified rates of 1 Hz for the CTD and the 2 Hz for the velocity sensor. The relative sample rate factor of exactly 0.500 s trivialized the mapping to a common time base.

Errors in derived ocean velocity arise from several sources. A fin on the profiler aligns the velocity sensor into the current to minimize the effect of wakes generated by the moving profiler. Faster relative speeds between the ocean and profiler reduce wake errors because the wake is more quickly advected away from the sensor. The primary effect is on periods smaller than about 10 s (appendix B). Errors also result from errors in ice velocity caused by errors in GPS fixes or interpolation in time of the 1-h ice velocity record to the time of the ITP-V observations. These GPS errors do not affect the estimated vertical velocity or turbulent fluctuations that involve removing a sample mean velocity, which constitute many of the results and analysis in this study. Errors in heading, pitch, and roll of the profiler may also be present, even after calibrations are applied. A bias of  $6^\circ$  in the ITP-V heading corresponds to a bias in the absolute ocean velocity of  $0.01 \text{ m s}^{-1}$  for a horizontal velocity of  $0.1 \text{ m s}^{-1}$ . For fixed-depth sampling, pitch and roll typically did not vary by more than  $3^\circ$  during each 40-min sampling period, while variations in heading were larger. Errors in heading do not affect vertical velocity fluctuations. During profiles, errors in pitch, roll, and heading will cause the motion of the profiler along the wire to be incorrectly accounted for and so result in errors in velocity. Overall, the observations support the conclusion that the derived ocean velocity is trustworthy.

## APPENDIX B

### Dominant Scales of Turbulent Fluctuations

Turbulent fluctuations are first considered as a function of frequency. Fourier coefficients for  $u$  and  $w$ , which contribute to one component of the turbulent vertical momentum flux, are calculated from each approximately 40-min record (e.g., Fig. B1) after the mean and trend are removed. When averaged over the 6-month record, squared coherence shows that the vertical and horizontal velocity fluctuations were significantly

correlated at all frequencies (Fig. B2a). Cospectra, which show the frequency distribution of only the fluctuations that are correlated, were elevated at periods of about 100–200 s, corresponding to ocean turbulence, and at periods less than about 10 s, corresponding to noise in the observations, possibly from eddies shed by the sensor (Thwaites et al. 2011; Fig. B2b). Coherence and cospectra between vertical velocity and the temperature or salinity fluctuations were similar in character to those with the horizontal velocity (not shown).

Dominant length scales are determined from cospectra as a function of the horizontal wavenumber (horizontal wavenumber is derived in section 2c using the relative velocity past the sensor). To eliminate high-frequency noise, Fourier coefficients for each 40-min record are calculated for wavenumbers that correspond to frequencies less than 0.1 cps. Cospectra are then calculated and averaged in wavenumber bins for the largest and smallest 50% of relative velocities past the sensor (Fig. B2c). A dominant peak is evident near 10–50-m scales for the larger relative velocities and near 5–30-m scales for the smaller relative velocities. With a 40-min sampling period, a mean relative velocity of  $0.02 \text{ m s}^{-1}$  is required to observe a 50-m scale; the mean relative velocity exceeded  $0.02 \text{ m s}^{-1}$  in 90% of the fixed-depth observations. Because smaller relative velocities were associated with smaller dominant scales, the ITP-V observations capture the dominant scales in all cases.

#### REFERENCES

- Cairns, J. L., and G. O. Williams, 1976: Internal wave observations from a midwater float, 2. *J. Geophys. Res.*, **81** (12), 1943–1950.
- D'Asaro, E. A., and M. D. Morehead, 1991: Internal waves and velocity fine structure in the Arctic Ocean. *J. Geophys. Res.*, **96** (C7), 12 725–12 738.
- Ekman, V. W., 1905: On the influence of the earth's rotation on ocean-currents. *Ark. Mat., Astron. Fys.*, **2**, 1–52.
- Fer, I., and A. Sundfjord, 2007: Observations of upper ocean boundary layer dynamics in the marginal ice zone. *J. Geophys. Res.*, **112**, C04012, doi:10.1029/2005JC003428.
- Gregg, M. C., and E. Kunze, 1991: Internal wave shear and strain in Santa Monica Basin. *J. Geophys. Res.*, **96** (C9), 16 709–16 719.
- Gross, T. G., and A. R. M. Norwell, 1985: Spectral scaling in a tidal boundary layer. *J. Phys. Oceanogr.*, **15**, 496–508.
- Halle, C., and R. Pinkel, 2003: Internal wave variability in the Beaufort Sea during the winter of 1993/1994. *J. Geophys. Res.*, **108**, 3210, doi:10.1029/2000JC000703.
- Hunkins, K., 1966: Ekman drift currents in the Arctic Ocean. *Deep-Sea Res.*, **13**, 607–620.
- Huntley, D. A., 1988: A modified inertial dissipation method for estimating seabed stresses at low Reynolds numbers, with application to wave/current boundary layer mechanisms. *J. Phys. Oceanogr.*, **18**, 339–346.
- Jackson, J. M., E. C. Carmack, F. A. McLaughlin, S. E. Allen, and R. G. Ingram, 2010: Identification, characterization, and change of the near-surface temperature maximum in the Canada Basin, 1993–2008. *J. Geophys. Res.*, **115**, C05021, doi:10.1029/2009JC005265.
- Kalnay, and Coauthors, 1996: The NCEP/NCAR 40-Year Reanalysis Project. *Bull. Amer. Meteor. Soc.*, **77**, 437–470.
- Krishfield, R., J. Toole, A. Proshutinsky, and M.-L. Timmermans, 2008a: Automated Ice-Tethered Profilers for seawater observations under pack ice in all seasons. *J. Atmos. Oceanic Technol.*, **25**, 2091–2105.
- , —, and M.-L. Timmermans, 2008b: ITP data processing procedures. Woods Hole Oceanographic Institute Tech Rep., 24 pp. [Available online at <http://www.whoi.edu/fileserver.do?id=35803&pt=2&p=41486>.]
- Levine, M. D., C. A. Paulson, and J. H. Morison, 1985: Internal waves in the Arctic Ocean: Comparison with lower-latitude observations. *J. Phys. Oceanogr.*, **15**, 800–809.
- Lu, P., Z. Li, B. Cheng, and M. Lepparanta, 2011: A parameterization of the ice–ocean drag coefficient. *J. Geophys. Res.*, **116**, C07019, doi:10.1029/2010JC006878.
- Maykut, G. A., and M. G. McPhee, 1995: Solar heating of the Arctic mixed layer. *J. Geophys. Res.*, **100** (C12), 24 691–24 703.
- McPhee, M. G., 1979: The effect of the oceanic boundary layer on the mean drift of pack ice: Application of a simple model. *J. Phys. Oceanogr.*, **9**, 388–400.
- , 1987: A time-dependent model for turbulent transfer in a stratified oceanic boundary layer. *J. Geophys. Res.*, **92** (C7), 6977–6986.
- , 1992: Turbulent heat flux in the upper ocean under sea ice. *J. Geophys. Res.*, **97** (C4), 5365–5379.
- , 1994: On the turbulent mixing length in the oceanic boundary layer. *J. Phys. Oceanogr.*, **24**, 2014–2031.
- , 2002: Turbulent stress at the ice/ocean interface and bottom surface hydraulic roughness during the SHEBA drift. *J. Geophys. Res.*, **107**, 8037, doi:10.1029/2000JC000633.
- , 2004: A spectral technique for estimating turbulent stress, scalar flux magnitude, and eddy viscosity in the ocean boundary layer under pack ice. *J. Phys. Oceanogr.*, **34**, 2180–2188.
- , 2008a: Physics of early summer ice/ocean exchanges in the western Weddell Sea during ISPOL. *Deep-Sea Res. II*, **55**, 1075–1097.
- , 2008b: *Air–Ice–Ocean Interaction: Turbulent Ocean Boundary Layer Exchange Processes*. Springer, 226 pp.
- , 2012: Advances in understanding ice–ocean stress during and since AIDJEX. *Cold Reg. Sci. Technol.*, **76–77**, 24–36.
- , and L. H. Kantha, 1989: Generation of internal waves by sea ice. *J. Geophys. Res.*, **94** (C3), 3287–3302.
- , and D. G. Martinson, 1994: Turbulent mixing under drifting pack ice in the Weddell Sea. *Science*, **263**, 218–221.
- , and T. P. Stanton, 1996: Turbulence in the statically unstable oceanic boundary layer under Arctic leads. *J. Geophys. Res.*, **101** (C3), 6409–6428.
- , and J. H. Morison, 2001: Under-ice boundary layer. *Encyclopedia of Ocean Sciences*, J. H. Steele et al., Eds., Elsevier, 3069–3076.
- , T. Kikuchi, J. H. Morison, and T. P. Stanton, 2003: Ocean-to-ice heat flux at the North Pole environmental observatory. *Geophys. Res. Lett.*, **30**, 2274, doi:10.1029/2003GL018580.
- , J. H. Morison, and F. Nilsen, 2008: Revisiting heat and salt exchange at the ice–ocean interface: Ocean flux and modeling considerations. *J. Geophys. Res.*, **113**, C06014, doi:10.1029/2007JC004383.
- , R. Skogseth, F. Nilsen, and L. H. Smedsrud, 2013: Creation and tidal advection of a cold salinity front in Storfjorden:

2. Supercooling induced by turbulent mixing of cold water. *J. Geophys. Res. Oceans*, **118**, 3737–3751, doi:10.1002/jgrc.20261.
- Merrifield, M. A., and R. Pinkel, 1996: Inertial currents in the Beaufort Sea: Observations of response to wind and shear. *J. Geophys. Res.*, **101** (C3), 6577–6590.
- Morison, J. H., M. G. McPhee, and G. A. Maykut, 1987: Boundary layer, upper ocean, and ice observations in the Greenland Sea marginal ice zone. *J. Geophys. Res.*, **92** (C7), 6987–7011.
- Notz, D., M. G. McPhee, M. G. Worster, G. A. Maykut, K. H. Schlunzen, and H. Eicken, 2003: Impact of underwater-ice evolution on Arctic summer sea ice. *J. Geophys. Res.*, **108**, 3223, doi:10.1029/2001JC001173.
- Perovich, D. K., and J. A. Richter-Menge, 2009: Loss of sea ice in the Arctic. *Annu. Rev. Mar. Sci.*, **1**, 417–441.
- Pinkel, R., 2005: Near-inertial wave propagation in the western Arctic. *J. Phys. Oceanogr.*, **35**, 645–665.
- Rudnick, D. L., and S. T. Cole, 2011: On sampling the ocean using underwater gliders. *J. Geophys. Res.*, **116**, C08010, doi:10.1029/2010JC006849.
- Shaw, W. J., T. P. Stanton, M. G. McPhee, and T. Kikuchi, 2008: Estimates of surface roughness length in heterogeneous under-ice boundary layers. *J. Geophys. Res.*, **113**, C06012, doi:10.1029/2007JC004550.
- Shirasawa, K., and R. G. Ingram, 1991: Characteristics of the turbulent oceanic boundary layer under sea ice. Part 1: A review of the ice–ocean boundary layer. *J. Mar. Syst.*, **2**, 153–160.
- Sirevaag, A., M. G. McPhee, J. H. Morison, W. J. Shaw, and T. P. Stanton, 2010: Wintertime mixed layer measurements at Maud Rise, Weddell Sea. *J. Geophys. Res.*, **115**, C02009, doi:10.1029/2008JC005141.
- , S. de la Rosa, I. Fer, M. Nicolaus, M. Tjernstrom, and M. G. McPhee, 2011: Mixing, heat fluxes and heat content evolution of the Arctic Ocean mixed layer. *Ocean Sci.*, **7**, 335–349.
- Tennekes, H., and J. L. Lumley, 1972: *A First Course in Turbulence*. MIT Press, 314 pp.
- Thwaites, F. T., and A. J. Williams, 1996: Development of a modular acoustic velocity sensor. *Proc. OCEANS '96: Prospects for the 21st Century*, 2, Fort Lauderdale, FL, MTS/IEEE, 607–612, doi:10.1109/OCEANS.1996.568296.
- , R. Krishfield, M.-L. Timmermans, J. M. Toole, and A. J. Williams, 2011: Noise in ice-tethered profiler and McLane moored profiler velocity measurements. *Proc. 2011 IEEE/EOS 10th Current, Waves and Turbulence Measurements Workshop*, Monterey, CA, IEEE Oceanic Engineering Society, 205–212, doi:10.1109/CWTM.2011.5759553.
- Timmermans, M.-L., S. T. Cole, and J. M. Toole, 2012: Horizontal density structure and restratification of the Arctic Ocean surface layer. *J. Phys. Oceanogr.*, **42**, 659–668.
- Toole, J. M., M.-L. Timmermans, D. K. Perovich, R. A. Krishfield, A. Proshutinsky, and J. A. Richter-Menge, 2010: Influences of the ocean surface mixed layer and thermohaline stratification on Arctic sea ice in the central Canada Basin. *J. Geophys. Res.*, **115**, C10018, doi:10.1029/2009JC005660.
- Williams, A. J., F. T. Thwaites, A. T. Morrison, J. M. Toole, and R. Krishfield, 2010: Motion tracking in an acoustic point-measurement current meter. *Proc. OCEANS 2010 IEEE*, Sydney, Australia, IEEE, 1–8, doi:10.1109/OCEANSSYD.2010.5603862.